CellPress

Neuron
Primer

# Pushing the Boundaries of Neuroimaging with Optoacoustics

Saak V. Ovsepian,[1,2,3,*] Ivan Olefir,[1,2] Gil Westmeyer,[1,4,5] Daniel Razansky,[1,2] and Vasilis Ntziachristos[1,2,*]
[1]Institute for Biological and Medical Imaging, Helmholtz Zentrum Munich, German Research Center for Environmental Health, Ingolstaedtler Landstrasse 1, 85764 Neuherberg, Germany
[2]School of Medicine and Bioengineering, Technical University of Munich, 81675 Munich, Germany
[3]International Centre for Neurotherapeutics, Dublin City University, Dublin 9, Republic of Ireland
[4]Institute of Developmental Genetics, Helmholtz Zentrum München, 85764 Neuherberg, Germany
[5]Department of Nuclear Medicine, Technical University of Munich, 81675 Munich, Germany
*Correspondence: saak.ovsepian@gmail.com (S.V.O.), v.ntziachristos@tum.de (V.N.)
https://doi.org/10.1016/j.neuron.2017.10.022

**With the central ability to visualize a variety of endogenous chromophores and biomarkers or exogenous contrast agents, optoacoustic (photoacoustic) imaging empowers new experimental capabilities for investigating brain mechanisms and functions. Here, the operational principles of optoacoustic neuroimaging are reviewed in conjunction with recent advances enabling high-resolution and real-time observation, which extend beyond the reach of optical imaging methods. Multiple implementations of optoacoustics for monitoring hemodynamics and neuro-vascular responses in the brain are showcased. The unique capabilities of optoacoustic imaging for multi-spectral cellular and molecular sensing are discussed with reference to recent application for visualizing healthy and diseased brains. Outstanding challenges in the field are considered in the context of current and future applications of optoacoustic neuroimaging for basic and translational neuroscience research. In pushing the boundaries of brain imaging, optoacoustic methods afford major insights into the neuronal mechanisms of brain functions and organization of behavior.**

## Introduction

Advances in physics, engineering, computer science, and biotechnology have prompted sweeping innovations in neuroimaging, with enormous potential for elucidating the fundamental relation between the structure and function of the nervous system. Structural imaging of the brain in its modern sense dates back more than a century to the founders of neurology and neuroscience research, such as P. Broca, A. Mosso, S. Ramon-y-Cajal, E. Moniz, and others (Raichle, 1998; Zago et al., 2012). Over many decades, physicians and physiologists have also recognized the premises for functional brain imaging, with C. Sherrington and co-workers observing first that experimentally induced changes in neuronal activity are associated with alterations in the color of brain tissue (Roy and Sherrington, 1890). An impressive range of tools and technologies have been developed and widely used for both structural and functional brain imaging (Yang and Yuste, 2017; Yuste and Konnerth, 2005), which includes optical intrinsic signal (OIS) imaging (Gratton et al., 2017; Grinvald et al., 1999), optical microscopy, and, in particular, confocal (CFM) and multiphoton microscopy (TPM) (Helmchen and Denk, 2005; Svoboda and Yasuda, 2006), magnetic resonance imaging (MRI) (Logothetis, 2008; Ogawa et al., 1990), positron emission tomography (PET) (Cabeza and Nyberg, 1997; Posner and Raichle, 1998), and X-ray computer tomography (X-CT) (Hoeffner et al., 2012; Raichle, 1998).

Owing to their excellent sensitivity and penetration depth, PET and especially MRI have found extensive implementations in brain imaging, enabling visualization of the organization and a variety of processes and functions within deep brain tissue, through the intact skull. The applicability of MRI and PET for animal research also enables investigations in the laboratory, advantageous for interrogation of various disease models. Despite major pluses in structural, functional, and molecular brain imaging, both MRI and PET have limited temporal resolution, are costly and involve substantial infrastructure investment, and, therefore, are not currently accessible for routine research and pre-clinical applications. Due to small brain size and the disruptive effects of the skull on the magnetic field, the spatial resolution of MRI in mouse studies is also compromised (Hoyer et al., 2014; Koch and Reid, 2012). Indeed, contrasting the 1,450 mL human brain, the mouse brain is only 0.5–0.6 mL. As a result, in typical human neuroimaging application, a voxel could contain 3–4 mL tissue as compared to 0.003–0.004 mL in mice. Because the signal-to-noise ratio (SNR) of MRI is directly proportional to the voxel size, contrast achieved with a 3-Tesla human scanner exceeds that of animal measurements in a 9.4-Tesla scanner by a factor of 5. Although the limited spatial resolution can be balanced by repeated image acquisition, this comes with a further loss in temporal resolution, with doubling of SNR quadrupling the imaging time. Noteworthy, the increase in the magnetic field strength also affects the relaxation parameters of MRI contrast, intensifying field inhomogeneity and energy absorption (Farahani et al., 1990; Hoyer et al., 2014; Yang et al., 1997), while smaller voxel size amplifies the physiological noise caused by breathing and heartbeat. Last, but not least, the reliance of PET (and MRI for certain applications) on exogenous tracers to achieve specific information also necessitates invasive procedures, entailing health and safety risks (Gu et al., 2013; Ibaraki et al., 2004; Kennan et al., 2002).

Conversely, optical methods have been more accessible to biomedical research and preclinical studies. Microscopic methods, such as CFM and especially TPM, are used with great success for basic and translational brain research in model animals to visualize the structure and function of neurons and glia at superb temporal and spatial resolution *in vivo* and *ex vivo*, sensing processes at the level of individual neurons and subcellular structures (George, 2010; Katona et al., 2012; Ouzounov et al., 2017; Sofroniew et al., 2016; Yu et al., 2005). In most applications, these studies use contrast agents or genetically encoded reporter proteins to observe the finer details of cellular architecture and investigate functional and molecular processes in the brain and to capture resting and stimulation-induced neuronal activities (Figure 1A). With such implementations, major advances have been made in deciphering a wide range of processes and functions, ranging from imaging neuronal axons and presynaptic boutons to dendritic spine in healthy and diseased brains, to elucidating the characteristics of $Ca^{2+}$ signals and voltage dynamics in different neuronal groups (Busche et al., 2008; Chen et al., 2011; Grienberger and Konnerth, 2012; Peterka et al., 2011). A critical shortage of optical microscopy, and especially *in vivo* microscopic brain imaging, is the limited observation field and sub-millimeter penetration, with the latter being due to strong scattering of incident photons by the skull and brain tissue (Jacques, 2013; Ntziachristos, 2010; Ntziachristos et al., 2005). To overcome some of these limitations, the majority of microscopic brain imaging studies employed invasive procedures involving partial or complete removal of the scalp and skull or implantation of cranial windows (Burgold et al., 2011; Filser et al., 2015; Meyer-Luehmann et al., 2008). Progress in developing fluorescence dyes and reporter proteins combined with high NA optics, better detectors, and signal multiplexing recently enabled subcellular resolution *in vivo* brain imaging of extended field of view and depths > 1 mm (Ouzounov et al., 2017; Yang and Yuste, 2017). Through the use of light-weight miniaturized epifluorescence scopes with optoelectronic components and GRIN lens, fiberscopes, or miniaturized two-photon microscopes, cellular and subcellular resolution functional brain imaging of behaving mice has been also attained (Flusberg et al., 2008; Ghosh et al., 2011; Rivera et al., 2011; Szabo et al., 2014). Nevertheless, the fundamental constraints set by light diffraction limits the non-invasive, high-resolution optical microscopy to superficial observations with restricted field of view (Ntziachristos, 2010).

Macroscopic optical imaging has also been considered for visualizing brain function, taking advantage of its superb ability for label-free sensing of hemodynamic and metabolic changes over different brain regions (Hillman, 2007; Ntziachristos, 2010). With epi-illumination, the capability of optical imaging to capture weighted signal from the brain surface was showcased in rodents and humans (Ma et al., 2009; Martin et al., 2006; White et al., 2011) (Figure 1B). In conjunction with carefully controlled stimuli, changes in hemoglobin gradients and blood flow in response to sensory inputs have been observed, with tight coupling between the activity of neurons and hemodynamic changes in different brain regions demonstrated (Devor et al., 2003; Dunn et al., 2003; Hillman, 2007, 2014). Using diffuse near-infrared (NIR) illumination, the feasibility of non-invasive optical macroscopy with measurements of brain activity in humans has been explicitly shown (Boas et al., 2004; Eggebrecht et al., 2014; Gratton et al., 2017; Ntziachristos et al., 1999). In all these applications, the ability to penetrate deeper than optical microscopy comes with major constraints on the spatial resolution achieved. By looking deeper in the tissue (beyond 1 mm), the effects of photon scattering become stronger and degrade the image quality and resolution, which complicate the quantification and interpretation of experimental measurements.

Optoacoustic (photoacoustic) imaging has emerged recently as a powerful interrogation method capable of overcoming the major drawbacks of conventional high-resolution optical imaging. It bridges the depth limits of ballistic optical microscopy and the resolution limits of diffuse optical imaging. The method detects ultrasound waves generated by endogenous tissue chromophores and/or exogenous reporters in response to incident light absorption (Figure 1C), which prompts local heat production (in the milli-K range) with thermoelastic expansion, generating pressure ultrasound waves measured using transducers. The performance of optoacoustic imaging, therefore, unlike traditional optical imaging methods, is not constrained by photon scattering but by diffraction of ultrasound waves (Ntziachristos et al., 2005; Oraevsky et al., 1999; Taruttis and Ntziachristos, 2015; Wang and Hu, 2012). Table 1 summarizes the key characteristics of the multispectral optoacoustic tomography (MSOT; mesoscopic and macroscopic) and optoacoustic microscopy (OAM) in comparison to other biological imaging modalities. Because sound propagating through tissue is scattered orders of magnitude weaker than photons, optoacoustic imaging achieves better spatial resolution in deeper tissue compared to customary optical imaging. Figure 1C schematizes the operational principle of optoacoustic brain imaging and presents representative examples. With the addition of multispectral capabilities, optoacoustics enables the detection and spectral decomposition of endogenous chromophores and exogenous agents, provided they attain absorption spectra that can be distinguished from each other (Dima et al., 2014; Ntziachristos and Razansky, 2010; Taruttis and Ntziachristos, 2015). Such unique characteristics of optoacoustic imaging have already proven highly useful for interrogating a wide range of processes and functions unfolding in living organisms, specific tissue types, and organs, including the nervous system (Hu, 2016; Lutzweiler and Razansky, 2013; Taruttis et al., 2015; Yao and Wang, 2014).

In the following sections, we outline key features of optoacoustic imaging and illustrate their recent implementation for neuroscience research. We discuss topical studies of neural dynamics and brain function that use optoacoustic methods to resolve hemodynamic gradients and the functional load of different brain structures at rest and under stimulation. We review the latest applications of multispectral optoacoustic imaging for sensing neural activity and mapping the distribution of contrast agents in the brain and discuss major recent developments in exploring neurological disease. Finally, we summarize outstanding challenges in the field and project on the future basic and translational applications of optoacoustic neuroimaging.

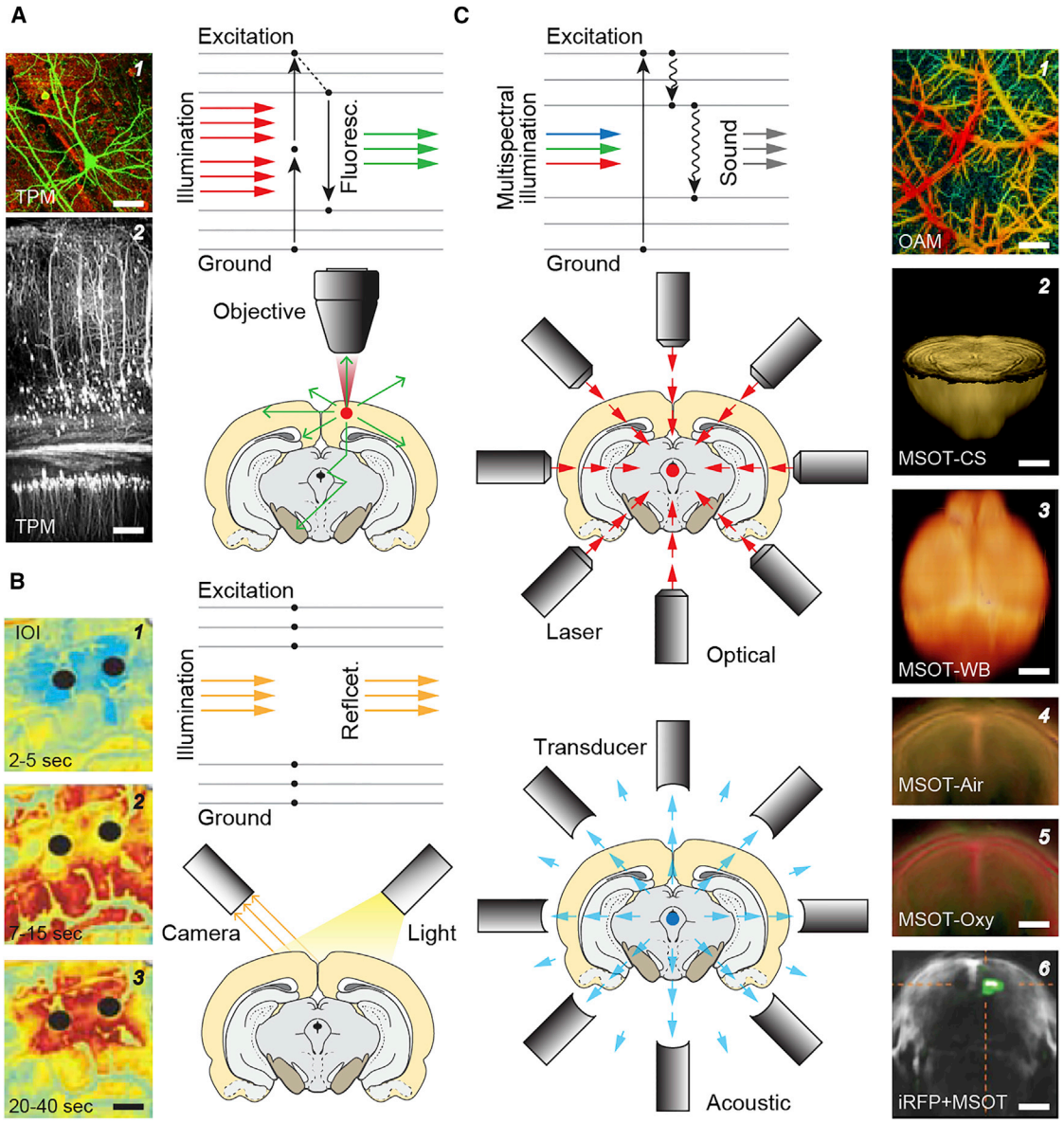


**Figure 1. Operational Principles of Two-Photon Microscopy, Optical Intrinsic Signal Imaging, and Multispectral Optoacoustic Tomography**
Schematics illustrating the operational principles, imaging penetration depth, and contrast mechanisms of two-photon microscopy (TPM) (A), optical intrinsic signal (OIS) imaging (B), and multispectral optoacoustic tomography (MSOT) (C) with representative images. Unlike optical (absorption or refraction) imaging mechanisms of TPM (A, 1 and 2) or OIS (B, 1, 2, and 3), imaging with optoacoustic methods utilizes ultrasound signals generated by non-radiative relaxation of excited chromophores for image formation (C, 1–6). Images: (A) (1) *In vivo* TPM micrograph of a GFP expressing cortical pyramidal cell (courtesy by Mr. K. Berry, Nedivi laboratory at MIT); (2) *in vivo* TPM image of cortical pyramidal neurons of YFP-H mouse (courtesy of Dr. R. Kawakami, Dr. T. Hibi, and Dr. T. Nemoto, Hokkaido University); (B) (1–3) average images of the raw OIS imaging data taken from the human brain showing changes of the $HbO_2$ levels at three time points after cortical stimulation with alternating current through electrodes (black circles) (adapted with permission from Ma et al., 2009); (C) (1) microscopic optoacoustic image of the Hb concentrations in the norm-oxygenated mouse cerebral cortex (adapted with permission from Cao et al., 2017); (2 and 3) 3D reconstructed anatomical MSOT image of a mouse brain *ex vivo* acquired at 740 nm wavelength: coronal and dorsal views, respectively (I.O., S.V.O., and V.N.); (4 and 5) color-coded relative $sO_2$ maps of the mouse brain *in vivo* during air- and 100% oxygen-breathing phases overlaid with anatomical MSOT images (adapted with permission from Olefir et al., 2016); (6) single-wavelength anatomical optoacoustic image of a mouse brain overlaid with unmixed MSOT of iRFP U-87 expressing glioblastoma tumor implant (adapted with permission from Deliolanis et al., 2014). Note that unlike TPM and OIS imaging, which are limited to the surface of a specimen (<1 mm), optoacoustic imaging enables visualization of the entire mouse brain.

## Principles and Modalities of Optoacoustic Imaging

The sporadic use of optoacoustic methods for biological imaging dates back to the 1970s and early 1980s when it was considered for absorption spectroscopy, subsurface biological imaging, and sensing bio-materials (Rosencwaig, 1973, 1982). The recognition of highly advantageous biomedical imaging capacities of the optoacoustics was initially slow but expedited in the 1990s (Hoelen et al., 1998; Kruger et al., 1995; Oraevsky et al., 1999)

**Table 1. Comparison of the Performance of the MSOT and Optoacoustic Microscopy with Other Biological Imaging Modalities**

| | Contrast | Resolution (μm) | Penetration depth | Sensitivity (molar) | Toxicity | Accessibility |
|---|---|---|---|---|---|---|
| MSOT | ● | > 20 | ◐ | nano | ◐ | ● |
| OAM | ● | < 1 | ◔ | pico | ◔ | ● |
| Confocal | ● | < 1 | ○ | pico | ◔ | ◔ |
| 2P / MP | ● | < 1 | ◔ | pico | ◐ | ◐ |
| OCT | ◐ | > 1000 | ◔ | nano | ○ | ● |
| X-CT | ◔ | ~ 50 | ● | micro | ● | ◔ |
| MRI | ● | ~ 20 | ● | nano | ○ | ◐ |
| PET | ● | > 1000 | ● | femto | ◐ | ◔ |
| US | ○ | ~ 50 | ◔ | pico | ○ | ● |

Low High

2P/MP, two-photon/multiphoton microscopy; OCT, optical coherence tomography; X-CT, X-ray computer tomography; MRI, magnetic resonance imaging; PET, positron-emission tomography; US, ultrasound; MSOT, multispectral optoacoustic tomography (mesoscopic and microscopic); OAM, optoacoustic microscopy.

and 2000s (Ntziachristos et al., 2005; Razansky et al., 2007; Wang et al., 2003). Propelled by technological progress, to date, optoacoustic imaging enables real-time multi-wavelength illumination (Buehler et al., 2010, 2013; Razansky et al., 2011) and advanced imaging performance through adept tomographic methods, making possible new detection capacities and improving the sensitivity and spatial/temporal resolutions of imaging systems (Taruttis and Ntziachristos, 2015). Referred to as MSOT, this latest implementation utilizes multi-wavelength illumination with spectral unmixing algorithms for high-resolution sensing a variety of chromophores in biological specimens. The advantages of multispectral optoacoustic imaging over other means of *in vivo* optical interrogation of deep tissue have been already demonstrated in several biomedical imaging fields, including cancer research (Herzog et al., 2012; Laufer et al., 2012; Ruan et al., 2013), cardiovascular disease (Needles et al., 2013; Taruttis et al., 2012), pharmacokinetics (Bézière and Ntziachristos, 2015; Lutzweiler et al., 2014; Razansky et al., 2012), and neuroscience (Burton et al., 2013; Olefir et al., 2016; Yao et al., 2013). Together with unique capacities for multi-dimensional imaging, these developments pushed the boundaries of optoacoustic sensing beyond the reach of traditional optical imaging methods.

Optoacoustic imaging is fundamentally a three-dimensional method that, similar to ultrasonography, uses acoustic waves for image formation. However, in optoacoustics, the image formation differs from ultrasonography in terms of signal source, image content, and underlying contrast mechanisms. Traditional pulse-echo ultrasonography relies on acoustic impedance mismatches between different soft tissues to present structural features. In optoacoustic imaging, the contrast is produced by light-absorbing tissue chromophores and exogenous contrast agents, giving rise to broadband ultrasound waves, thus making it suitable for capturing selective structural, functional, and molecular features of the specimen of interest (Taruttis et al., 2015). Similar to optical imaging, in optoacoustic interrogation, one of the key strategies for deeper penetration has been the use of NIR light for illumination. This is largely because the predominant light absorbers in living samples, such as hemoglobin, water, and lipid, have their lowest absorption coefficient in the NIR (650–900 nm) region.

Based on the illumination and detection arrangements, three general classes of optoacoustic imaging have been defined (Ntziachristos, 2010). The first class, referred to as "optoacoustic macroscopy," capitalizes on the unique ability of optoacoustic imaging to perform high-resolution optical imaging deep within the biological specimen (Ntziachristos, 2010; Taruttis and Ntziachristos, 2015). In typical applications of this modality, illumination is afforded in the NIR using high-energy (>10 mJ) light pulses in the nanosecond range and delivered over a wide interrogation area (non-focused beam). Detection is performed in the 0.1–10 MHz range, achieving resolutions in the order of one to a few hundred microns, with the penetration depth reaching several centimeters. The second class, "optoacoustic mesoscopy," uses the same principle of operation but employs transducers in the 5–200 MHz range (Aguirre et al., 2017; Schwarz et al., 2017). Illumination, in this case, may be achieved with lower energies than in macroscopy, with penetration of several millimeters and a typical resolution within the sub-100 micron range. Recently, <10 μm axial resolution (mesoscopic) has been achieved at 4 mm imaging depth (Chekkoury et al., 2016; Omar et al., 2014; Soliman et al., 2015). The third class of optoacoustic imaging, known as "optoacoustic microscopy," utilizes a different principle of illumination—by scanning a

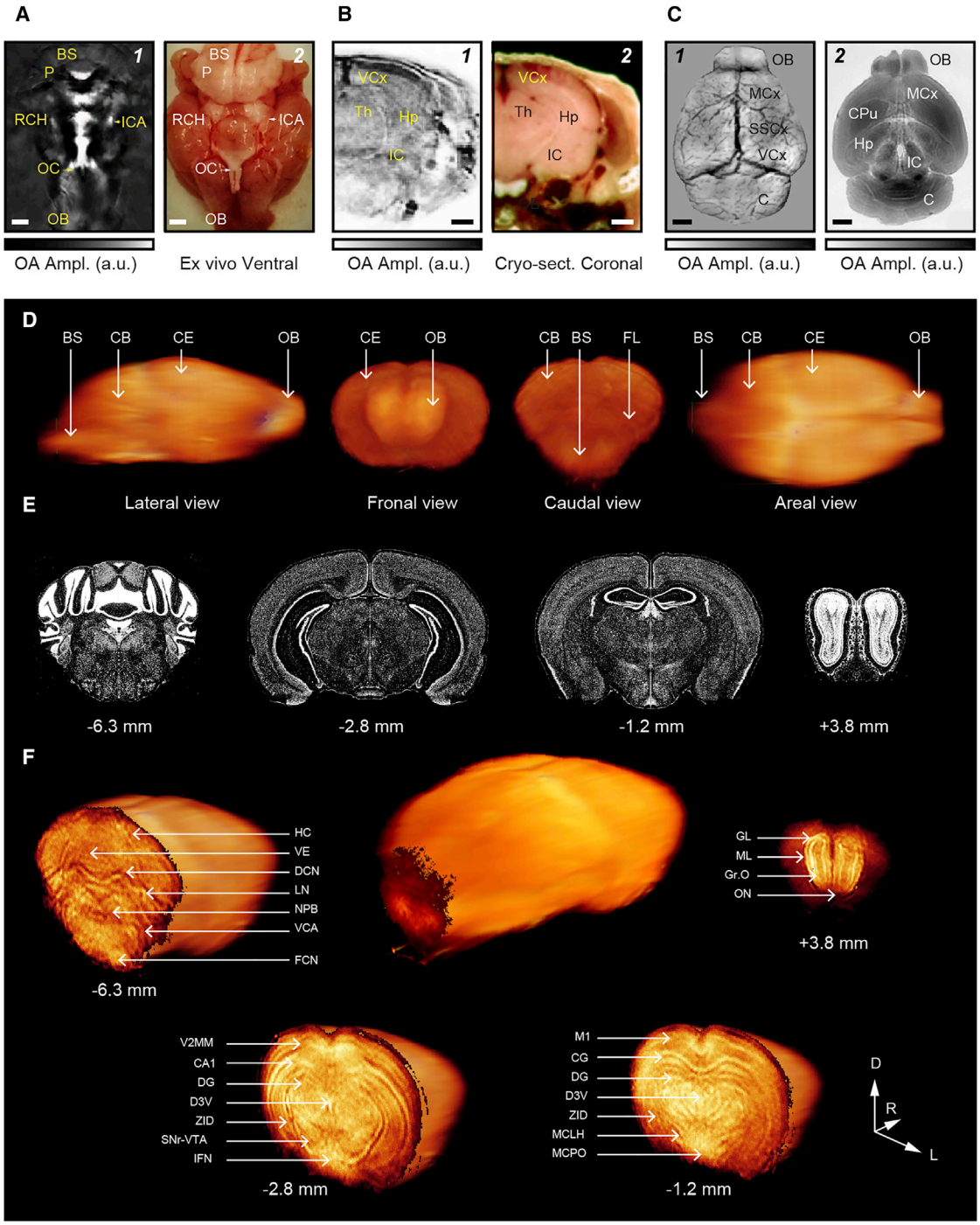


**Figure 2. Elucidating Brain Structure with Optoacoustic Tomography**

(A) *In vivo* optoacoustic image of the rat brain base acquired in tomographic regime with corresponding *ex vivo* photograph of the anatomy of the same brain (1 and 2, respectively). BS, brain stem; P, pons; RCH, right cerebral hemisphere; ICA, internal carotid artery; OC, optical cyasm; OB, olfactory bulb. Scale bar, 1 mm. Adapted with permission from Lin et al., 2015.

(B) Optoacoustic cross-section of the mouse brain (coronal plane) *in vivo* with the corresponding photograph of post-mortem cryosection (1 and 2, respectively). VCx, visual cortex; Th, thalamus; Hp, hippocampus; IC, internal capsule. Scale bar, 1 mm (from Olefir et al., 2016).

(C) *In vivo* imaging of the mouse brain through the intact skull (0.5 mm beneath the skull) with horizontal cross-sectional optoacoustic tomography and *ex vivo* image of the same mouse brain at 2.8 mm depth (1 and 2, respectively). OB, olfactory bulb; MCx, motor cortex; SSCx, somatosensory cortex; VCx, visual cortex; C, cerebellum; CPu, caudate putamen; Hp, hippocampus; IC, inferior colliculus. Scale bar, 1 mm. Adapted with permission from Li et al., 2016.

(D) An optoacoustic overview of the mouse brain *ex vivo*: four projections (lateral, frontal, caudal, and areal views). BS, brain stem; CB, cerebellum; CE, cerebrum; OB, olfactory bulb; FL, flocculus.

*(legend continued on next page)*

focused beam of the pulsed laser over the specimen—to collect generated sound waves from a spatially confined spot (volume element). With such an arrangement, images are formed by placing the measurements collected from each volume element onto a raster. In this imaging configuration, no tomographic techniques are necessary for image formation. The performance of optoacoustic microscopy, therefore, does not differ from conventional optical microscopy and is limited in terms of penetration to about 1 mm in scattering tissues, with a constrained field of view. Also, the resolution of optoacoustic microscopy, in this case, is determined by optical diffraction as opposed to ultrasound diffraction in optoacoustic macroscopy and mesoscopy. It is important to note that in addition to spectral and dynamic features, optoacoustics can also offer a continuum of imaging resolution and depth, i.e., high scalability (Ntziachristos, 2010; Wang and Hu, 2012). From a technology standpoint, optoacoustic macroscopy can be readily switched into mesoscopy by using ultrasonic detectors with a higher central frequency and wider bandwidth (Zemp et al., 2007; Zhang et al., 2009). Likewise, switching from optoacoustic mesoscopy to macroscopy using low-frequency detectors is possible with reducing the center frequency of the transducer, extending the imaging depth, and relaxing the spatial resolution (Song and Wang, 2007). In certain implementations, when optical focusing becomes gradually inefficient with increasing imaging depth, mesoscopic resolution optoacoustic imaging can be achieved with optoacoustic microscope (Estrada et al., 2014; Xing et al., 2013). Although the use of hybrid optoacoustic imaging modalities have been reported (Xia et al., 2013b; Xing et al., 2013), at present, switching between all modalities remains challenging and requires further engineering. In the following, different optoacoustic imaging implementations are discussed and showcased in various neuroimaging studies.

## Elucidating Brain Structure with Optoacoustic Imaging

The majority of optoacoustic neuroimaging reports focused on functional readouts from the brain, capitalizing on the superb light absorption by hemoglobin. Nevertheless, several studies also utilized other endogenous chromophores as contrast for structural imaging and visualization of deep vascular elements of the brain. Using acoustic signal detection within a few MHz range, optoacoustic macroscopy with NIR illumination proved capable of achieving 100–300 μm resolution at penetrations extending several millimeters. In this capacity, optoacoustic imaging was applied for acquisition of anatomical references, as well mapping functional and molecular processes in the intact brain of murine models, through the intact skin and skull (Burton et al., 2013; Deliolanis et al., 2014; Gottschalk et al., 2017; Kircher et al., 2012). Upon external illumination, cross-sectional brain images at different coronal planes revealed distinct structural features at a single (800 nm) wavelength. Structures such as the superior sagittal sinus, the third ventricle, and the posterior cerebral arteries could be observed deep within the mouse brain (Burton et al., 2013; Olefir et al., 2016; Razansky et al., 2011). The use of internal illumination through the oral cavity, on the other hand, enabled visualization of the basal vascular system of the rat brain, including Willis Circle with anterior and internal carotid arteries (Lin et al., 2015). Fine structural details of the ventral aspects of the cerebral hemispheres and brain stem, as well as the hypothalamus, olfactory lobes, cerebral medulla, and optical chiasm, have also been revealed (Figure 2A). With external 256- and 512-element ring array, hybrid optoacoustic-ultrasound structural images of the mouse brain were acquired recently and correlated with those obtained with histology (Olefir et al., 2016) (Figure 2B). Strong light absorption by vascular elements could be enhanced further by administration of exogenous contrast agents, such as indocyanine green (ICG), or direct injection of NIR-liposome-AuNR into the brain, further enriching the anatomical content of the structural features (Burton et al., 2013; Deliolanis et al., 2014; Lozano et al., 2012).

Mitigation of the effects of blood (hemoglobin) and especially the skull was shown using perfusion or partial removal of the skull bones, improving the quality and the resolution of label-free macroscopic images of the mouse brain (Li et al., 2016), making visible features afforded by water, cytochrome, lipid, and melanin absorption. Structures such as the central gray, cerebellum, cerebral aqueduct, corpus callosum, hippocampus, hypothalamus, neocortex, olfactory bulb, and lateral ventricles could be distinguished on reconstructed images (Li et al., 2016) (Figure 2C). Using spectral decomposition algorithms, endogenous chromophores by virtue of their optical absorption could also be discerned. In saline-perfused brains, multispectral optoacoustic imaging within the 480–680 nm range revealed distinct anatomical features, which originate mainly from cytochrome b and c, while the lipid-rich white matter tracts sharpened the contours of major subcortical nuclei and formations. Extending the multispectral analysis of brain structure over the NIR, a wealth of additional details of brain structure have been revealed recently, demonstrating the unprecedented imaging capabilities of MSOT along with the ability to reveal fine anatomical details within cortical and subcortical compartments of the mouse brain (I.O, S.V.O., and V.N., unpublished data). Figure 2 presents macroscopic MSOT images of the mouse brain with details closely matching to those captured with customary histological methods (Figures 2D–2F).

The abundance of lipids in the nervous system with distinct spectral signature and absorption peaks at 930 and 1,210 nm (second overtone of abundant C-H bonds) renders it particularly useful for structural MSOT of the brain. In the mouse brain, by dry weight, gray matter has 55%–60% protein and 35%–40% lipid,

(E) Histological cross-sections of the mouse brain stained with a Nissl method corresponding to the anatomical optoacoustic planes shown beneath (caudal-rostral direction from left to right; millimeters from Bregma) (courtesy of Allan Brain Institute).
(F) 3D reconstruction of the adult mouse brain imaged *ex vivo* at 740 nm (middle) with four cross-sections corresponding to above shown histological planes. Note close match of structural features in optoacoustic cross-sections with histology. D, R, and L, dorsal, rostral, and lateral, respectively; HC, hemisphere cerebelli; VE, vermis; DCN, deep cerebellar nuclei; LN, lateral cerebellar nucleus; NPB, medial parabrachial nucleus; VCA, ventral cochlear nucleus; FCN, facial nucleus; V2MM, secondary visual cortex, medio-medial; CA1, hippocampal CA1 area; DG, dentate gyrus; D3V, dorsal third ventricle; ZID, zona incerta dorsal; SNr, substantia nigra reticulate; VTA, ventral tegmental area; IFN, inter-fascicular nucleus; M1, motor cortex 1; CG, cingulum; MCLH, magnocellular lateral hypothalamus; MCPO, magnocellular preoptic nucleus; GL, glomeruli; ML, mitral cell layer; Gr.O., a granular layer of the olfactory bulb; ON, olfactory nerve.

while myelin contains 70%–85% lipid and 15%–20% protein (Siegel et al., 2006). Considerable differences in protein and lipid content in different brain compartments, hence, would constructively enhance the image formation *in vivo* if the hemoglobin signal could be lessened. The successful use of optoacoustic mesoscopy for imaging peripheral myelinated nerves of swine and mice *ex vivo* (Mari et al., 2014; Matthews et al., 2014) suggests the viability of lipid-based neuroimaging for analysis of myelinated nerves and potentially central tracts *in vivo* in the context of brain development and demyelination disease (Compston and Coles, 2008; Fernandez et al., 2015). Taking advantage of NIR-III absorption of lipids by C-H bonds (1,720 nm), a single transducer (20 MHz) imaging was used for sensing myelinated white matter bundles and tracking loss of myelin after contusive injury in the rat spinal cord *ex vivo* (Wu et al., 2014). The post-injury recovery of myelinated spinal cord white matter under treatment with a neuroprotective agent ferulic-acid-conjugated glycol chitosan (FA-GC) was also demonstrated, inferring bond-selective imaging of lipid as a valuable assay for myelin detection with optoacoustics.

In the context of label-free structural brain imaging, it is worth noting that several neuronal types are enriched with neuron-specific chromophores, such as neuromelanin and neuroferritin, which, with high-sensitive spectral decomposition methods, could be potentially used as a contrast source for anatomical, molecular, and developmental studies. In particular, neuromelanin deposits in catecholaminergic neurons of the basal ganglia and midbrain nuclei can render these structures suitable for longitudinal studies of neurodegenerative disease affecting the viability of these neurons. Likewise, deposits of neuroferritin in large neurons of the globus pallidus and especially the parvocellular red nucleus could enable sensing these key extrapyramidal hubs. Interestingly, the feasibility of optoacoustic lipofuscin imaging, another endogenous chromophore enriched in neurons, was shown recently with the use of avalanche photodetector; the pigmented retinal epithelium of rat and human was observed with distribution of melanin and lipofuscin mapped at high resolution (Zhang et al., 2010, 2011).

## Monitoring Hemodynamics and Oxygenation of Brain Tissue at Multiple Scales

Despite the emerging new and exciting utilities of optoacoustics for structural brain imaging, the ability to resolve hemoglobin distribution and dynamics in real time at multiple scales is the main catalyst for its neuroimaging applications. Most of our understanding of brain mechanisms is based on electrophysiological readouts from selectively sampled neurons in partial or complete isolation, i.e., outside of their physiological environment. As a highly complex and self-organizing system, the mammalian brain operates simultaneously at myriads of scales and dimensions, extending from minuscule clusters of synapses and dendritic spines to neuronal groups and further to large-scale neural networks (Buzsáki, 2010; Mesulam, 1998; Mountcastle, 1997). Due to inherent scalability, optoacoustic imaging is uniquely suitable for multiscale functional brain studies, exploiting hemoglobin as the principal source of the contrast (Figures 3A–3C).

A constant supply of oxygen and nutrients is vital for neuronal survival and performance. The circulation with oxygen supply to the brain tissue, therefore, must be maintained at adequate levels, with increase in neuronal activity and oxygen demand triggering a focal rush of blood (Raichle, 1998; Roy and Sherrington, 1890). The activity-dependent enhancement of blood flow and oxygen supply, however, is typically greater than required, resulting in a transient decrease in the amount of deoxygenated hemoglobin (Hb) (Fox et al., 1988; Malonek et al., 1997; Malonek and Grinvald, 1996). This peculiar but highly advantageous feature, which underlies the blood-oxygen-level-dependent (BOLD) signal, is used in functional MRI (fMRI) of the brain (Attwell et al., 2010; Attwell and Iadecola, 2002; Hillman, 2014; Logothetis, 2008; Ogawa et al., 1990). As label-free fMRI detects only paramagnetic Hb (i.e., oxygen free), it cannot distinguish the decreased blood perfusion from the increased blood oxygenation. The ability of optoacoustic imaging to decompose Hb from oxygenated hemoglobin ($HbO_2$) and quantify them with unprecedented accuracy enables measurements of oxygen saturation ($sO_2$) of biological tissue without ambiguities related to blood volume changes (Laufer et al., 2007). Indeed, with some approximations, changes in $sO_2$ can be measured with ±1% precision. Using measurements at two or more wavelengths, it is possible to distinguish between different oxygenation states of hemoglobin, producing spatial and temporal maps of sO2 dynamics (Herzog et al., 2012; Li et al., 2008), with accuracy of measurements in deep tissue proportional to the number of wavelengths employed (Tzoumas et al., 2015).

Dynamics of hemoglobin gradients proved useful for monitoring changes in tissue oxygenation over extended brain areas using optoacoustic macroscopy. Burton and colleagues applied MSOT to analyze changes in Hb, $HbO_2$, and $sO_2$ on cross-sections of the entire mouse brain *in vivo* before and during breathing gas challenges (Figures 3D and 3E). Images acquired at different planes revealed fluctuations in Hb absorption in the superior sagittal sinus and posterior cerebral arteries as well as several other prominent cerebral vessels (Burton et al., 2013). With the continuous acquisition of multispectral data and spectral decomposition of $HbO_2$ and Hb, variations in hemoglobin absorption across the entire brain were shown to be tightly related to the composition of supplied breathing gas (Burton et al., 2013). The same report analyzed the perfusion and clearance rates of systemically administered ICG in the brain of intact mouse. A similar imaging configuration was used for measurements of the rate of regional oxygenation changes and comparison of the readouts before and after gas challenge, with oxygen saturation rates within the somatosensory cortex found to exceed those in feeding vessels; the latter implies tighter coupling of the oxygenation of cortical tissue with the breathing state (Olefir et al., 2016). Using a similar experimental paradigm but different imaging protocols, five-dimensional optoacoustic data were acquired recently from mice subjected to hyperoxia and normoxia, with hemodynamic parameters such as blood oxygenation, total hemoglobin, cerebral blood volume, Hb, and $HbO_2$ measured in real time (Gottschalk et al., 2015). Earlier, a single-element circular scanning ultrasonic transducer (Wang et al., 2003) or a stationary multi-element transducer array (Li et al., 2010; Yao and Wang, 2014) was used for macroscopic imaging of the hemodynamics in the cerebral cortex. The utility of optoacoustic macroscopy for

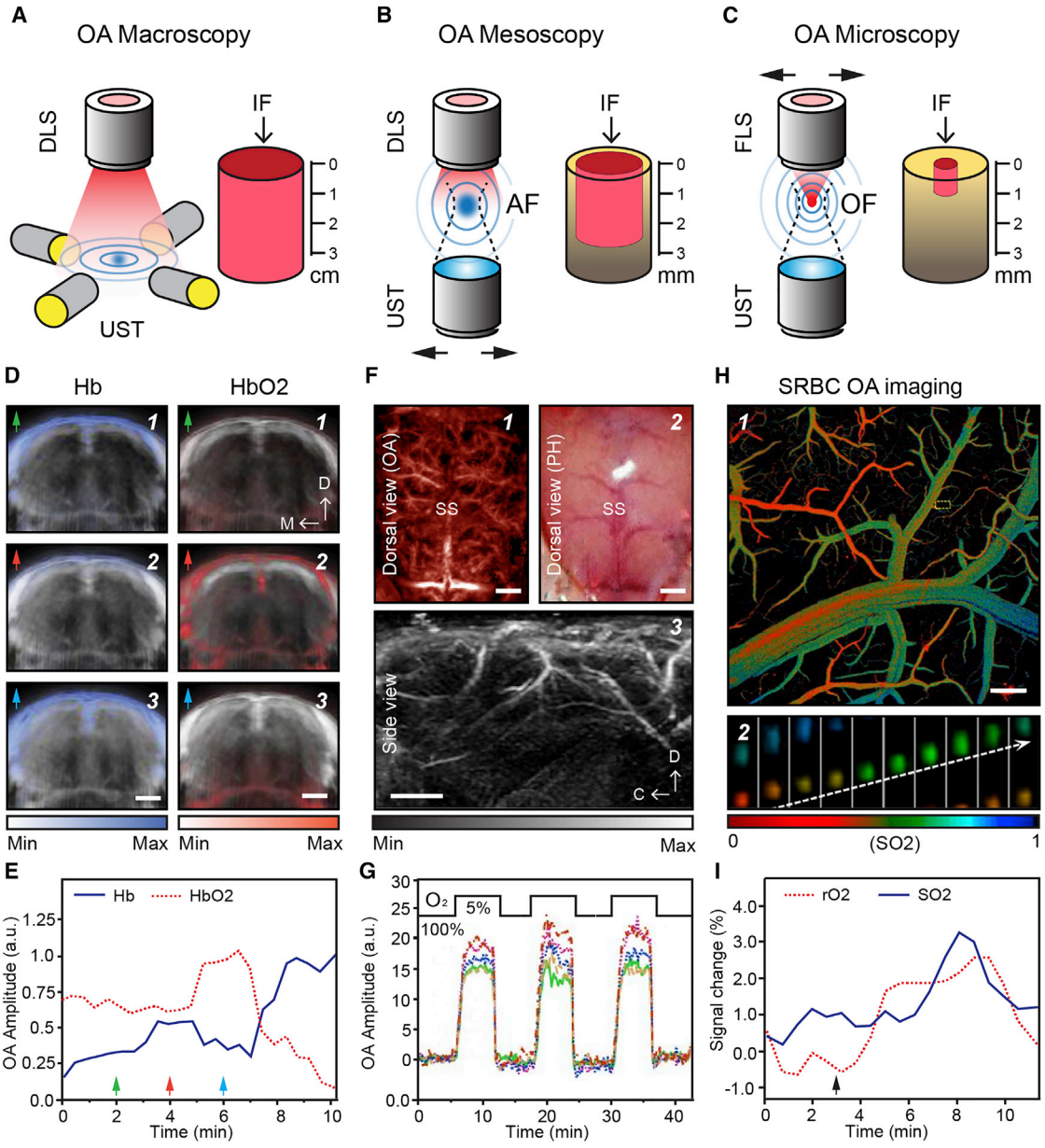


**Figure 3. Multi-scale Optoacoustic Functional Brain Imaging**

(A–C) Graphical representation of the illumination and detection schemes of optoacoustic macroscopy (A), mesoscopy (B), and microscopy (C). Note the modality-dependent variations in the imaging resolution and depth (right schematic). DLS, diffuse light source; UST, ultrasound transducer; IF, imaging field; AF, acoustic focus; OF, optical focus. Double arrows indicate the scanning module of the imaging system.

(D) Macroscopic (MSOT) images of the changes in Hb and $HbO_2$ levels in the mouse brain induced by hypoxia and hyperoxia. From top to bottom: pseudo-colored Hb and $HbO_2$ maps acquired during the supply of a normal air followed by a mixture of air with 10% $CO_2$ (green arrow), 100% $O_2$ (red arrow), and 100% $CO_2$ (blue arrow) overlaid with the anatomical image. Scale bars, 1 mm.

(E) The time course of the changes in Hb and $HbO_2$ signals in response to alterations of the breathing gas mixtures (Burton et al., 2013).

(F) Noninvasive *in vivo* optoacoustic mesoscopic image of the mouse cortex vasculature (1) with a photograph of the same area after removal of the skull (2). SS, sagittal sinus. Scale bars, 1 mm. 3D optoacoustic image of the vasculature in the mouse brain obtained using an excitation wavelength of 590 nm (3). Parasagittal view, maximum intensity projection. Scale bar, 0.5 mm.

(G) Dynamic blood vessel responses acquired through a hypoxic challenge shown, reflective of changes of ratiometric optoacoustic signals at 561 and 570 nm. Each colored trace represents a respective cortical vessel. Adapted with permission from Laufer et al. (2009), Stein et al. (2009b), and Xia et al. (2013a).

(H) Representative microscopic $sO_2$ image of the mouse visual cortex (top) with sequential snapshots of single red blood cell (SRBC) releasing oxygen in a mouse cortex (bottom) (1 and 2). Scale bar, 200 μm. Blood flows from left to right. The dashed arrow follows the trajectory of a single flowing red blood cell.

(I) Graphical representation of the transient responses of SRBCs within the visual cortex to a single stimulus (semi-rectangle, bottom inset); black arrow, visual stimulation; $sO_2$, oxygen saturation; $rO_2$, oxygen release rate (Wang et al., 2013).

transcranial visualization of the brain in larger animals, such as monkeys and sheep, was also shown (Petrov et al., 2012; Yang and Wang, 2008), with transcranial detection of changes in the cerebral blood oxygenation in sheep proven to be feasible (Petrov et al., 2012; Yang and Wang, 2008). In the later study, specifically designed photon recycler has been used to facilitate the delivery of sufficient light through the thick skull and scalp.

Laufer and colleagues applied a Farby-Perot sensing interferometer for multispectral optoacoustic mesoscopy of an intact mouse brain vasculature *in vivo* (Laufer et al., 2009). High-resolution images of the large- and medium-size cerebral vasculature were obtained at different wavelengths (between 590 and 889 nm), demonstrating that the perfusion rate and hemoglobin dynamics can be visualized through the intact skull and skin, with maintained high contrast at depths up to 3.7 mm (Figure 3F). Through careful analysis of the illumination wavelengths and imaging depth, it was shown that with a longer wavelength, deeper structures can be clearly resolved. Nearly simultaneously, using the same imaging configuration but piezoelectric detectors, blood oxygenation was monitored noninvasively in the cortex of living mice under normoxia and hypoxia (Stein et al., 2009a, 2009b; Xia et al., 2013a) (Figures 3F and 3G). A pixel-wise normalization of the data acquired at Hb dominant (526 nm) and isosbestic (570 nm) wavelengths revealed a dramatic increase in the Hb signal in response to hypoxia. Major vascular hallmarks such as sagittal sinus, middle cerebral artery, and coronal suture were clearly identified and correlated with photographic images, proving the utility of optoacoustic mesoscopy for monitoring changes in oxygenation levels in several cortical vessels through the intact skull and skin. Liao and colleagues applied optoacoustic mesoscopy to quantify stimulus-induced changes in total Hb concentration, cerebral blood volume (CBV), and $sO_2$ as well as transient hemodynamic response in small cortical vessels in intact mice (Liao et al., 2012a, 2012b). Electrical stimulation of the mouse forepaw was applied to elicit neuronal activation in primary somatosensory cortex, while a large numerical aperture wideband ultrasound transducer (50 MHz) enabled the collection of transcranial optoacoustic signals from the extended cortical regions of interest. Under these settings, changes in Hb concentration, CBV, and sO2 induced by forepaw stimulation were resolved with 36–65 μm spatial resolution. Recently, a hybrid system was introduced for continuous meso- and microscopic imaging with a smooth transition from acoustic (140 μm) to optical (23 μm) resolution demonstrated (Estrada et al., 2014). With this system, transcranial imaging of the mouse brain through an intact skull was achieved, with a wide diameter range of cerebral microvasculature observed. The study presents a special design for hybrid optical and acoustic resolution optoacoustic microscopy and extends the imaging depth of optical resolution imaging by means of high numerical aperture (NA) acoustic focusing. It also demonstrated for the first time the feasibility of a smooth transition between optical resolution on the surface and acoustic resolution at greater depths within an intensely scattering brain tissue (Estrada et al., 2014).

In the microscopic regime, optoacoustic imaging was applied for monitoring vasomotor changes of brain micro-vessels in response to gas challenge and activity-dependent oxygenation states. The microvasculature of the superficial mouse cortex was resolved down to the level of large- and medium-size capillaries through the intact skull (Hu et al., 2009a). Hemoglobin dynamics under hypoxia have been found to correlate with the vasomotor response, with smaller venules showing fewer cross-sectional changes as compared to arterioles. Researchers from the same group also developed a new implementation for optoacoustic microscopy, referred as single red blood cell (SRBC) flowoxigraphy, capable of imaging $O_2$ release from a single red blood cell in brain tissue (Wang et al., 2013). With this method, oxygen saturation and hemoglobin concentration changes, as well as blood flow rates, were measured through a small cranial opening and correlated with oxygen release by a single red blood cell. Optoacoustic flowoxigraphy was confirmed to be capable of quantifying the coupling between neuronal activity and SRBC oxygen delivery under rest and sensory stimulation (Figures 3H and 3I). To appreciate better high-resolution imaging capabilities, depth resolving features of optoacoustic microscopy were compared with those of two-photon imaging *in vivo* (Yao et al., 2016). As in any high-resolution, depth-resolved optical imaging modality, with increase in imaging depth (~0.7 mm), optical scattering degrades both the lateral resolution and the contrast of optoacoustic images as expected for diffraction-limited optical imaging. Indeed, at a given wavelength, fine vasculature in deep brain tissue could be resolved by two-photon microscopy (800 nm) but not by optoacoustic imaging (532 nm).

Distortions induced by the murine skull and its impact on microscopic and mesoscopic imaging of brain vasculature has been studied in considerable detail by Kneipp and colleagues using a new optical and acoustic resolution optoacoustic microscope, which utilizes an ultra-wideband spherically focused single element Polyvinilidene fluoride (PVDF) 30 MHz transducer (Kneipp et al., 2016). For acoustic resolution studies, broad and unfocused illumination was applied via a liquid light guide illuminating the sample orthogonally or by means of a multimode fiber inserted through the central bore of the transducers aperture. With this method, diffraction-limited acoustic resolution of 48 μm/24 μm in the lateral and axial directions has been achieved. Optical resolution imaging of small vessels, on the other hand, has been attained by focusing the laser beam onto the surface of the sample using GRIN lens, yielding an optical focus FWHM of 20 μm. It has been shown that strong low-pass filtering of signals by the skull can significantly deteriorate the spatial resolution of deep tissue images, where no light focusing was possible. The image quality, however, can be improved using cranial windows and a thinning of the skull over the region of interest, which comes with drawbacks of invasive surgery and compromised integrity of the brain tissue, causing alterations of neuronal activity.

## Mapping Large-Scale Activity of Neuronal Assemblies

The ability to capture high-resolution volumetric images of large brain compartments or entire brain of small animals in real time is arguably the greatest asset of optoacoustic neuroimaging. After all, integrative functions of the brain and neural organization of behavior emerge from the coordinated activity of extended assemblies of neurons, with individual nerve cells interchangeably

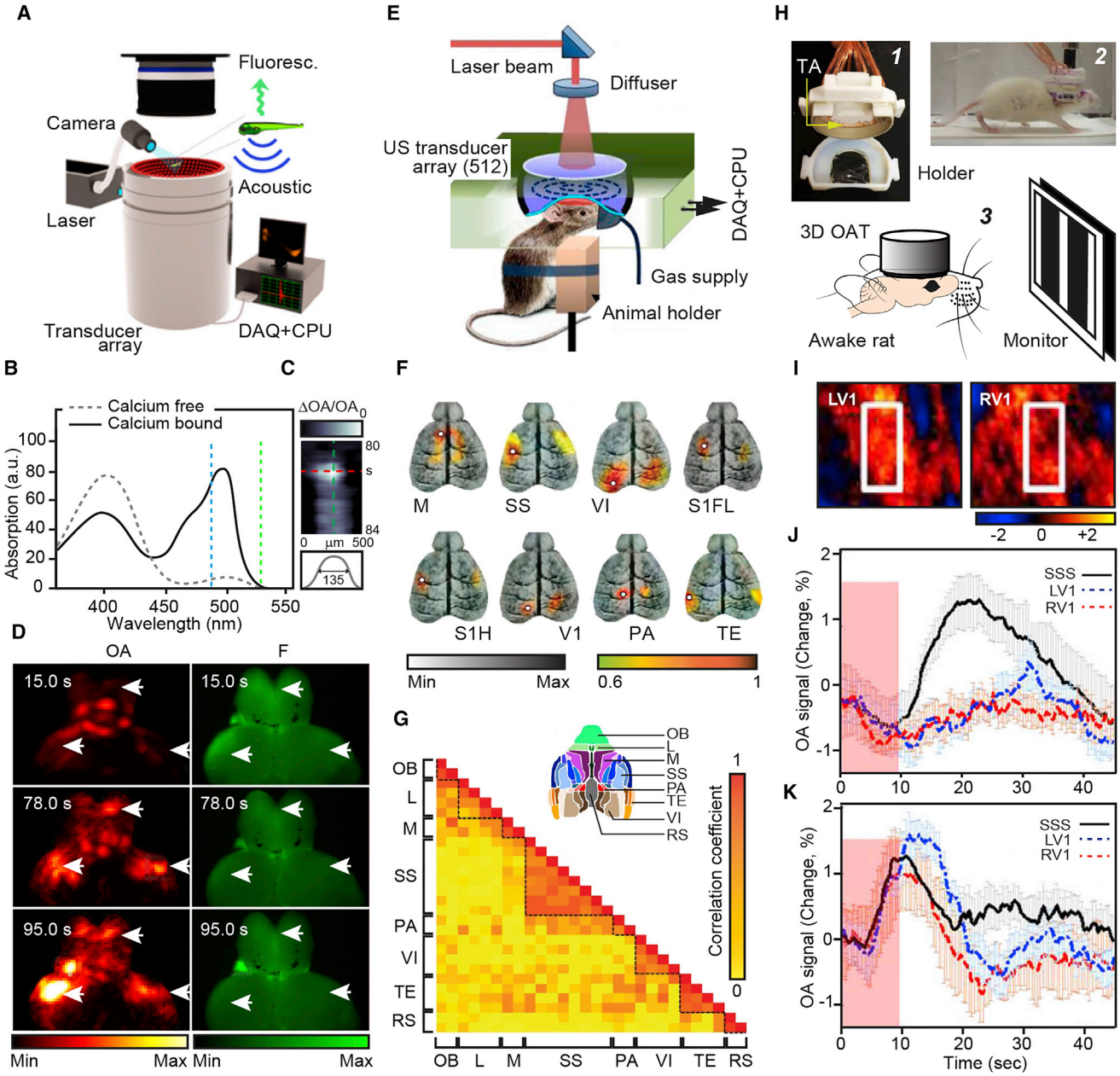


**Figure 4. Visualizing the Large-Scale Functional Dynamics of Brain Circuits with Optoacoustic Imaging**

(A) Schematic of the functional optoacoustic neuro-tomography (FONT) device utilized for whole zebrafish brain imaging.

(B and C) Demonstration of the spectral dependence of the absorbance of calcium-bound versus calcium-free GCaMP5G (B) and characterization of the spatial resolution of the optoacoustic $Ca^{2+}$ imaging platform (C), respectively.

(D) Volumetric optoacoustic (left) and planar epi-fluorescence (right) images of the zebrafish brain before (15.0 s) and after exposure of the fish to the neuro-stimulant agent (78.0 and 95.0 s). Note the enhanced localized activity captured by whole-brain optoacoustic tomography at several locations throughout the brain (left) versus less pronounced fluorescence signal due to intense light scattering (right). Adapted with permission from Dean-Ben et al. (2016).

(E and F) Schematic of the functional optoacoustic imaging system used for visualizing of the mouse brain connectome (E) and images of the resting state functional connectivity of a live mouse cortex acquired non-invasively (F), respectively. M, motor cortex; SS, somatosensory cortex; VI, visual cortex; S1FL, primary somatosensory forelimb area; S1H, somatosensory hind limb areas; V1, primary visual cortex; PAC, parietal cortex; TE, temporal cortex.

(G) Correlation maps of eight functional regions of the cerebral cortex with corresponding regions (inset). On correlation map, each row and each column correspond to a parcel. Dashed black lines were shown for added visualization. The regions and sub-regions indicated in the atlas are as follows: OB, olfactory bulb; L, limbic cortex; M, motor cortex; SS, somatosensory cortex; PA, parietal cortex; VI, visual cortex; TE, temporal cortex; RS, retro-splenial cortex. Adapted with permission from Nasiriavanaki et al. (2014).

(H) Volumetric optoacoustic imaging of the top layer of the visual cortex in behaving rats using a wearable optoacoustic device: (1) wearable transducer array (2) mounted on the head to behaving rat with (3) a monitor for visual input activation.

*(legend continued on next page)*

involved in different functional groups, reorganizing themselves in a constantly changing fashion (Buzsáki, 2006; Hebb, 2002). With central ability to visualize changes in hemoglobin gradients and sense dynamics of voltage- and calcium-sensitive dyes in real time, optoacoustic interrogation can afford unprecedented capabilities for exposing large-scale dynamics of brain circuits at multiple scales and dimensions in real time.

By combining fast, tunable lasers with advanced data processing algorithms and a transgenic approach, a method was developed recently for near real-time 3D functional optoacoustic neuro-tomography (FONT), capable of high-resolution imaging of spatial and spectral dynamics of $Ca^{2+}$ in neural circuits across the entire brain of the larvae and adult HuC:GCaMP5G zebrafish (Dean-Ben et al., 2016) (Figures 4A–4D). Two excitation wavelengths (488 nm and 530 nm) were utilized, which corresponds to the peak and close to zero absorption of the GCaMP5G fluorescence $Ca^{2+}$ reporter expressed in neurons. Optoacoustic measurements were compared with planar fluorescence readouts by combining the data acquired with the FONT system and fast sCMOS camera. A low level of neuronal activity was observed in resting larvae, which was rapidly and strongly enhanced by a potent neurostimulant pentylenetetrazole (PTZ). The strong correlation between the simultaneously acquired optoacoustic and fluorescence signals during pharmacologically stimulated neuronal activity confirmed that optoacoustic reads of the GCaMP5G signal can be used as a reliable indicative of neural dynamics within the intact brain. Distinct GCaMP5G signals were also registered in the isolated brain of an adult zebrafish, providing time-resolved 3D optoacoustic whole-brain images (Figure 4D). Comparison of the optoacoustic and fluorescence readouts showed much deeper penetration of the former with the ability to resolve $Ca^{2+}$ dynamics throughout the entire brain of the zebrafish. The unique facility of FONT to collect 100 volumetric frames/s across scalable fields ranging between 50 and 1,000 $mm^3$ at an impressive 35–200 μm resolution presents a major methodological advance for *in vivo* whole-brain imaging. With further advanced FONT systems and better-optimized transducers or super-resolution strategies, real-time functional optoacoustic interrogation of the entire brain of small animals at cellular and subcellular resolution is envisioned in the near future.

The ability to resolve Hb and $HbO_2$ endows optoacoustic imaging with a unique ability for complementary studies of hemodynamic and neurovascular coupling with neuronal activity, using $Ca^{2+}$, $Na^+$, $K^+$, and $Cl^-$ reporters, with no additional costs. The proof of concept for hemoglobin-based, non-invasive macroscopic imaging of the distributed activity of cortical circuits has been presented by Nasiriavanaki in imaging of the resting-state functional connectivity of the mouse cortex (Nasiriavanaki et al., 2014). Applying single-wavelength optoacoustic imaging (532 nm, the isosbestic wavelength of Hb and $HbO_2$), eight main functional regions of the neocortex with several sub-regions were distinguished at 150 μm in-plane resolution, with strong correlations of intra- and interhemispheric resting-state activity demonstrated (Figures 4E–4G). Both the pattern of brain activity and the extent of the correlation between various brain regions and sub-regions were highly sensitive to hypoxia, which caused decoupling of intra- and intercortical synchrony. Of note, subtle variations between activities of corresponding cortical fields of two hemispheres were also noted, suggesting lateralization of cortical functions in the resting mouse brain. The use of a single excitation wavelength by this study, however, does not allow distinction of $HbO_2$ and Hb; hence, in terms of gaining novel functional insights, it presents no major advance over the earlier results obtained in similar readings with the use of OIS imaging methods (Grinvald et al., 1986; White et al., 2011).

Other reports combined whole-brain optoacoustic mesoscopy with drug-induced acute epilepsy models to reconstruct the large-scale neural dynamics and to study properties of forebrain circuits involved in initiation, propagation, and termination of synchronous activity throughout various brain compartments *in vivo*. In anesthetized mice, for example, Gottschalk and colleagues utilized volumetric optoacoustic imaging of 4-amydopyrin (4-AP)-induced seizures and electroencephalography (EEG) to reconstruct the initiation and evolution of pathological hyperactivity in real time. Hot spots of seizures were visualized throughout the entire mouse brain and located to different cortical and subcortical structures. Shortly after administration of 4-AP, focal hyperactivity of brain circuits with hemodynamic changes was observed in thalamic circuits followed by recruitment of limbic and associative circuits (Gottschalk et al., 2017). Other researchers used a similar approach to monitor the PTZ-induced neuronal hyperactivity and associated hemodynamic response in the visual cortex and sagittal sinus of anesthetized and awake rats (Tang et al., 2015). Acute generalized tonic-clonic seizures were induced by intraperitoneal injection of PTZ (0.1 g/kg of body weight). In all animals, a robust increase in optoacoustic signal was observed, which was accompanied by EEG synchrony and freezing behaviors. Analysis of the time course of the PTZ-induced seizures showed that while in both groups the enhanced hemodynamic response in the cortex correlated with the injection of PTZ, in anesthetized rats the response has a longer latency and lower amplitude as compared to the awake animals. Interestingly, in both awake and anaesthetized rats, hemodynamic changes detected with optoacoustic imaging preceded the synchronized electrical discharges registered by EEG (~50 s for awake-moving state and ~90 s for anesthetized state), consistent with similar observations made with fMRI, near-infrared spectroscopy, and OIS imaging (Hawco et al., 2007; Osharina et al., 2010; Tenney et al., 2003). Changes in tissue perfusion associated with drug-induced seizure revealed with optoacoustics agree with the results of laser Doppler flowmetry and optical spectroscopic studies, which confirmed that the low Hb in seizure foci reflects the rush of oxygenated blood to hyperactive neural circuits (Harris et al., 2014; Zhao et al., 2011).

(I) Volumetric optoacoustic images of the visual cortex with analyzed regions of interest (in boxes). RV1, right primary visual cortex; LV1, left primary visual cortex. (J and K) Changes in optoacoustic signal reflective of the cerebral hemodynamic responses for RV1, LV1, and superior sagittal sinus (SSS): averaged data across nine trials superimposed with a SEM are plotted over time. The pink shading on individual graphs represents 10 s stimuli. Adapted with permission from Tang et al. (2016).

Recently, a portable miniaturized 3D optoacoustic imaging device has been developed, which allowed sensing and comparison of the evoked activity in the primary visual (V1) and associated circuits in awake behaving rats (Tang et al., 2015, 2016). Ring-type transducer arrays capable of mapping oxygen saturation at two wavelengths (710 and 840 nm) were utilized to register Hb and $HbO_2$ gradient maps and to deduce the $sO_2$ dynamics before and after a flash stimulus (Figures 4H–4K). As illustrated, a considerable increase in Hb signal was evident in the V1 area of both sides, as well as in the sagittal sinus, within 10 s of visual stimulation followed by slow recovery of the signal to the baseline level. The $HbO_2$ response, on the other hand, reacted less rigorously and showed an opposite directionality. While the results of these experiments are in agreement with high specificity and localized character of primary visual responses, the amplitude and temporal parameters of V1 activation suggest considerable case-by-case variability and require more detailed future studies.

### Multispectral Molecular Optoacoustic Neuroimaging

Non-invasive imaging of specific molecular targets, receptors, and biochemical processes *in vivo* are among the most sought-after capabilities in post-genomic biology and neuroscience (Holcman and Yuste, 2015; James and Gambhir, 2012; Weissleder and Ntziachristos, 2003). One of the key motivations of molecular imaging and sensing is translation of common *in vitro* bioassay strategies into *in vivo* setting in an attempt to overcome existing limitations. While *in vitro* techniques have long afforded valuable insights into the physiology and pathobiology at cellular and tissue levels, they fall short in providing analysis of similar processes in an intact organism over time, making it difficult to appreciate the full picture of physiological and pathological states and processes. Furthermore, *in vitro* studies are required to remove cells, tissue, or organ samples from their natural environment for research, which necessitates invasive procedures, chemical treatment, and fixation of samples (Gujrati et al., 2017; James and Gambhir, 2012; Taruttis et al., 2015; Weissleder and Pittet, 2008). Currently, there is a pressing need in effective methods that allow non-invasive studies of biochemical and molecular processes within intact organisms over time.

Intra-vital molecular optoacoustic imaging can be achieved using endo- and exogenous chromophores and reporters, with a selection of appropriate illumination and detection means, to attain specific absorption and sensing in deep tissue. Initial reports of success in molecular imaging with MSOT came from resolving DsRed and mCherry fluorescence proteins using small invertebrates and mouse models (Ma et al., 2012a, 2012b; Razansky et al., 2009b; Ye et al., 2012). Taking advantage of transgenic adult zebrafish expressing mCherry under the Gal-4/UAS promoter, Razansky and colleagues applied cross-sectional MSOT to visualize deep-seated structures within a highly scattering tissue environment (Razansky et al., 2009b). Based on the steep decline of the mCherry absorption and spectral decomposition, the vertebral column and inner organs of adult zebrafish have been analyzed and visualized at ~30 μm resolution. The strong enrichment of mCherry was detected in the upper spinal cord and in the hindbrain structures of the fish, an observation also verified by high-resolution inspections of post-mortem fixed tissue using fluorescence microscopy (Razansky et al., 2009b). Although the spatial resolution and SNR in this study was somewhat limited, the use of broadband acoustic detectors and super-resolution techniques are expected to improve the resolution and enhance the contrast of MSOT imaging in the foreseeable future.

Another report showcased the molecular imaging capabilities of MSOT using infrared fluorescent protein (iRFP) expressing U-87 malignant glioma (MG) glioblastoma implants in deep subcortical structures of the adult mouse brain (Deliolanis et al., 2014). Optoacoustic performance of several red-shifted proteins was characterized and compared with their fluorescence properties in fluorescence molecular tomography (FMT). In all comparative studies, MSOT proved superior, resolving the iRFP expressing U-87 MG glioblastoma with ~100 μm resolution, as confirmed with follow-up post-mortem histology and microscopy (Figures 5A–5C). Although the recovery of the bio-distribution of iRFP in the mouse brain was also possible with FMT, the image quality, resolution, and contrast achieved by MSOT on the same scans was considerably better. This is hardly surprising given that the performance of MSOT is affected in a lesser degree by photon scattering, which facilitates deeper penetration and ~100 μm in-plane resolution at depths of several millimeters (Ntziachristos, 2010; Ntziachristos and Razansky, 2010). Recently, MSOT studies were combined with switchable non-fluorescent phytochrome BphP1 proteins for imaging brain tumors in mice (Yao et al., 2016). Taking advantage of the red-shifted absorption of excited BphP1 with photo-convertibility, tumor growth and metastasis were monitored at close to 100 μm resolution (Figures 5D–5F). The use of genetically encoded tyrosine reporter system through expression of the tyrosinase for the inducible enrichment of non-melanogenic cells with melanin is another rapidly advancing area of molecular MSOT, showing promising results from studies of non-neural tissue (Paproski et al., 2014; Stritzker et al., 2013a, 2013b). The relevance of this approach for neuroimaging, however, remains to be demonstrated.

On the neurotransmitter and receptor imaging frontier, Mishra and colleagues recently applied MSOT for visualizing the activity of extracellular glutamate and NMDA receptors, taking advantage of the conjugates of competitive and non-competitive antagonists of NMDA receptors with heptamethine cyanine-derived optoacoustic probes (Sim et al., 2015). After verifying high-affinity binding of the material to NMDA receptors in cultured mouse motor neurons (NSC-34), contrast agents were injected into the mouse motor cortex *in vivo*. Using MSOT imaging, it was possible to retrieve not only highly localized activity of selected contrasts (e.g., L1) *in vivo*, but also show in 3D the reversibility of this interaction, closely related to changes of local glutamatergic activity (Sim et al., 2015). Specific enrichment of the glutamate sensor in the mouse motor cortex was confirmed by post-mortem cryoslicing and epifluorescence microscopy. The results of this report have laid a new roadmap for future volumetric investigations of glutamate activity within the intact brain, with the development of probes capable of visualizing synaptic transmission in the intact healthy and diseased brain.

Despite major advances in MSOT with numerous compelling features for functional and molecular brain imaging, currently,

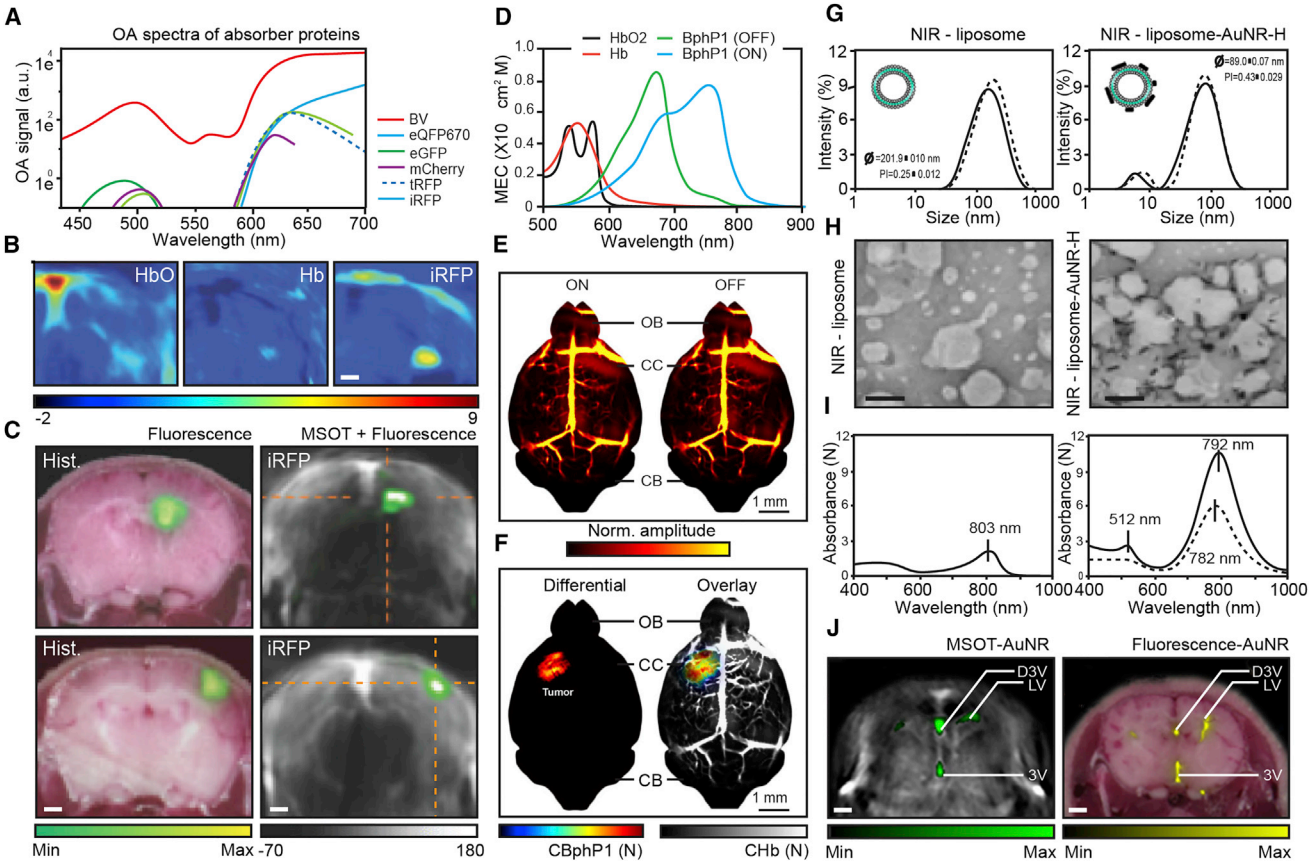


**Figure 5. Molecular Optoacoustic Neuroimaging**

(A) Near-infrared optoacoustic spectra of various fluorescence proteins (concentration: 2 μM) embedded at 8 mm depth in scattering tissue and a blood vessel (80% oxygen saturation, BV).

(B) Optoacoustic macrographic images depicting the three most prominent absorbers: $HbO_2$, Hb, and iRFP (iRFP expressing U-87 MG cells) detected in the mouse brain by spectral un-mixing.

(C) Representative optoacoustic images of iRFP expressing U-87 MG overlaid on histological and single-wavelength anatomical optoacoustic images. Adapted with permission from Deliolanis et al. (2014). Scale bar, 0.7 mm.

(D) Optical and optoacoustic characterization of non-fluorescent bacterial phytochrome BphP1. Molar extinction spectra of oxyhemoglobin ($HbO_2$), deoxyhemoglobin (Hb), BphP1 (ON), and BphP1 (OFF) are shown.

(E and F) The ON and OFF state optoacoustic images of a nude mouse brain *in vivo* acquired 2 weeks after grafting BphP1 expressing U87 tumor cells at ~3 mm underneath the surface. The tumor is invisible in either the ON state or the OFF state images due to the overwhelming background signals from the blood (E). The differential image, by contrast, shows the tumor by suppressing background signals (F). The overlay image shows the BphP1 signal in color and the background blood signal in gray. OB, olfactory bulb; CR, cerebrum; CB, cerebellum. Adapted with permission from Yao et al. (2016).

(G) Schematic of the structure and DLS particle size distribution of control NIR-liposome-AuNR and NIR-liposome-AuNR hybrid.

(H and I) TEM images of the material and UV-absorption spectra, respectively. Scale bar, 20 nm.

(J) MSOT image after injection of 5 μL of the hybrid material into the dorsal third ventricle (D3V) of the mouse brain. LV, lateral ventricle; 3V, third ventricle. The green overlay shows the signal detected from the AuNRs. The grayscale background is an optoacoustic image taken at 900 nm (left). The corresponding image is of cryosectioned brain tissue (right). The yellow overlay shows fluorescence detected from NIR-797. Scale bar, 0.7 mm. Adapted with permission from Lozano et al. (2012).

several factors hamper its widespread neuroimaging application. Improvements in the implementation of fast-tuning lasers and real-time data acquisition procedures are on their way (Dean-Ben et al., 2016; Gottschalk et al., 2015) along with enhanced sensitivity (Laufer et al., 2012; Razansky et al., 2009a; Winkler et al., 2013) and better contrast (Taruttis and Ntziachristos, 2015; Wilson et al., 2013) as well as spectral decomposition algorithms and methods (Glatz et al., 2011; Tzoumas et al., 2014, 2016). Developing new contrast agents for MSOT of the brain is of particular interest, with several new chromophores introduced and validated recently (Gujrati et al., 2017; Weber et al., 2016). Lozano and colleagues, for instance, produced and tested self-assembled liposome-gold hybrid nanorods and showcased their utility for imaging of the ventricular system of mouse brain *in vivo* (Lozano et al., 2012). After injection of the NIR-liposome-AuNR hybrids into the dorsal third ventricle, diffusion of the contrast agent and labeling of brain ventricles was confirmed using volumetric multispectral imaging with MSOT (Figures 5G–5J). High structural and colloidal stability and excellent multispectral optical properties of this formula offer the potentials for its application in multimodal *in vivo* brain imaging studies. On the same vein, tunable absorption of "smart" nanoparticles holds major promise for future basic and pre-clinical neuroimaging. Considerable efforts have been

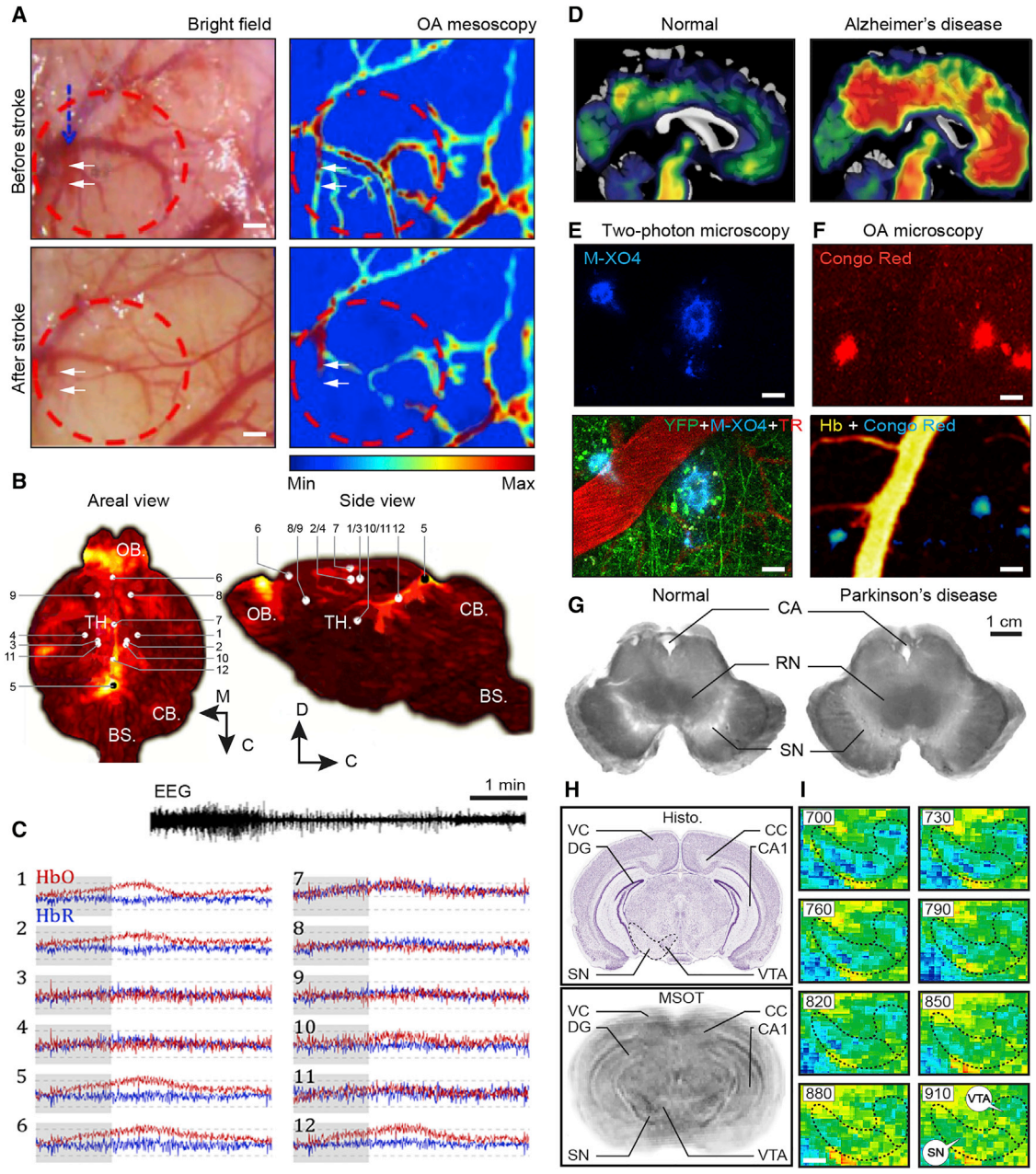


**Figure 6. Elucidating Brain Diseases with Optoacoustic Neuroimaging**

(A) Open-skull photograph of the cerebral cortical surface (left pair). The blue dashed arrow indicates the position for photothrombotic stroke; white double arrows point to the ablated artery. *In vivo* optoacoustic projection C-scan image of the corresponding cortical region with the blood vessels on the surface acquired at 570 nm. Scale bars, 100 μm. Adapted with permission from Liao et al. (2013a).

(B) Single voxel analysis of hemodynamic changes during epileptic seizures with maximum-intensity projections of $HbO_2$ distribution in the mouse brain and EEG recordings: a representative case. OB, olfactory bulb; CB, cerebellum; TH, thalamus; BS, brain stem.

(C) Time traces of Hb and $HbO_2$ changes from locations indicated in (B). Adapted with permission from Gottschalk et al. (2017).

(D) MRIs of the healthy and AD-affected human brains. Note heavy deposits of amyloid β (red) in the AD brain as compared to the absence of red signal in the age-matched healthy control; courtesy of B. Mander and M. Walker.

(E) High-resolution two-photon micrograph of amyloid β plaques in the APP/PS1d9 AD mouse brain (top, labeled with methoxy-XO4) and the same image overlaid with a two-photon angiogram (red, Texas red) and green neuropil (expressing YFP); courtesy of M. Meyer-Luehmann (bottom). Scale bars, 20 μm.

(F) Two-photon micrograph of amyloid plaques labeled with Congo red (top) and the same amyloid plaques visualized with optoacoustic microscopy (bottom). Scale bar, 200 μm. Adapted with permission from Hu et al. (2009b).

(G) Photographs of cross-sections of the midbrain of healthy and Parkinson's disease affected human brain demonstrating a loss of pigmented dopaminergic neurons of substantia nigra (SN); RN, red nucleus; CA, cerebral aqueduct. Courtesy of Robbins B, Neuropathology lab 2.

(H) Nissl-stained cross-section of the mouse brain corresponding to −3.3 mm plane of bregma (top) with the corresponding optoacoustic anatomical image of the same plane from the intact mouse brain *ex vivo* (bottom). Note strong absorption in the area corresponding anatomically to substantia nigra and ventral tegmental

*(legend continued on next page)*

also made toward improving contrast delivery means using physical and chemical opening of the blood-brain barrier (BBB) or through active transport systems of brain vasculature (Banks, 2016; Deng, 2010). Taking advantage of the physical opening of the BBB with mannitol, IRDye800-c conjugated with cyclic peptide cyclo(Lys-Arg-Gly-Asp-Phe) [c(KRGDf) for short] that targets integrin $\alpha_v\beta_3$ was delivered into the mouse brain to facilitate optoacoustic sensing of glioma implants overexpressing integrin $\alpha_v\beta_3$ receptors (Li et al., 2008; Wang et al., 2007). Likewise, $Gd^{3+}$-coated gold-silica-based nanoparticles capable of crossing the BBB were applied for enhanced transvascular delivery of contrast agents to the brain and triple MRI-optoacoustic-Raman imaging of glioblastoma in a mouse brain through an intact scalp and skull (Kircher et al., 2012). Finally, significant progress has been also reached recently in optimizing the intrathecal or retro-axonal transfer of contrast agents or reporters to the brain and spinal cord of animal models (Jain, 2012; Margrie et al., 2002; O'Leary et al., 2013; Ovsepian et al., 2015, 2016). Overall, these developments testify to highly promising molecular sensing capabilities of MSOT with its future implementations for high-resolution volumetric neuroimaging and suggest exciting opportunities ahead for preclinical neuroimaging in animal models with the prospect of therapeutic translations.

## Unleashing Optoacoustics for Elucidating Brain Diseases

Despite the remarkable progress in visualizing cellular and molecular processes, neuroscience still lacks a general theory as to how brain circuits operate and especially how their dysfunction can lead to a variety of neurological and neuropsychiatric disease. In his recent landmark paper, R. Yuste argues that the slow progress in understanding the brain as a whole may be in part due to inflated focus on single-neuron studies, which, despite propelling forward the fields of cellular and molecular neurobiology, has left circuits and their emergent properties less attended (Yuste, 2015). The arrival of novel imaging technologies capable of capturing the large-scale activity of neuronal circuit pinpointed brain areas involved in specific behaviors, mental states, or disease. Having the ability to sense and monitor neuronal activity and hemodynamics at multiple scales, optoacoustic neuroimaging has shown encouraging results in elucidating a wide range of brain disorders and diseases, including tumors and traumatic disorders, ischemia, stroke, seizures of various etiologies, and chronic neurodegenerative conditions.

Hemoglobin gradients have been utilized as the sole contrast in a vast majority of brain disease studies with optoacoustics, including tumors (Burton et al., 2013; Li et al., 2008; Staley et al., 2010), ischemia and stroke-related disruption of blood perfusion (Hu et al., 2011; Kneipp et al., 2014), and drug-induced seizures (Gottschalk et al., 2017; Tsytsarev et al., 2012; Zhang et al., 2008). In mice with U87 orthotopic glioblastoma implants into the corpus striatum, changes in hemoglobin distribution were visualized over several weeks using MSOT to determine and monitor the dynamics of tumor growth and related alterations in tissue oxygenation (Burton et al., 2013). Spectral decomposition and data analysis revealed strong localized hypoxia in the core of the tumor lesions. Discriminatory visualization of the tumor was possible using breathing gas challenge tests; whereas in mice supplied with 100% $O_2$ the tumor lesion area could not be demarcated clearly based on the hemoglobin signal, the tumor core became readily visible after increasing the $CO_2$ concentration (10%) in the breathing gas. Relating the volumetric MSOT data with results of post-mortem histology revealed a close match of the spatial distribution of the $HbO_2$ and the tumor labeled with specific IntegriSense 750, known to bind to angiogenic $\alpha_v\beta_3$ integrin receptors enriched in U87 cells (Burton et al., 2013).

Transient or lasting changes in the hemoglobin signal have also been used as the primary readout for brain ischemia imaging. Visualization of single cortical arterioles of the rat somatosensory cortex was combined with electrocorticography (ECoG) to monitor the effects of photothrombotic stroke on the cortical hemodynamic response induced by forepaw stimulation (Figure 6A). Through comparison of the functional optoacoustic imaging data with EEG recordings, alterations in Hb concentrations, blood volume, and $sO_2$ within the stroke region were mapped at ~50 μm resolution, shedding light on changes in vascular and metabolic reactions therein due to ablation of a small feeding arteriole (Liao et al., 2012a, 2013b). Others combined optoacoustic microscopy with transient obstruction of the middle cerebral artery to monitor adaptations in hemodynamic response at the level of microvessels and capillaries (Hu et al., 2011). A significant drop in $HbO_2$ was detected within the microvessel system downstream to the feeder artery as well as in the core of the stroke and draining veins. After reperfusion, arterial oxygen saturation in the affected area recovered to baseline levels while venous oxygen increased above the baseline, suggesting infarction of the neural tissue. Razansky and colleagues applied real-time whole-brain optoacoustic imaging of stroke-related perfusion deficit and widespread ischemia resultant of the occlusion of the middle cerebral artery in mice (Kneipp et al., 2014). Strong asymmetry of Hb distribution with regional hypoxia was observed on the entire brain cross-sections in the hemisphere affected by the transient ischemic event. Notably, MSOT images also captured mild hemodynamic disturbance reflective of the penumbra in the tissue surrounding the necrotic core, a valuable asset for demarcation of the ischemic tissue from the necrotic lesion.

Sensing inflammation and changes in the water content of the affected brain tissue is another useful application of *in vivo* optoacoustic neuroimaging, highly valuable for probing the functional state of microcirculation, edema, and post-traumatic recovery (Guevara et al., 2013; Xu et al., 2011; Yang et al., 2007). Using an experimentally induced inflammation model caused by lipopolysaccharide (LPS) injections (Duncan et al., 2006), a significant decrease in tissue oxygenation was observed in the brain

regions of the midbrain enriched with neuromelanin. VE, visual cortex; DG, dentate gyrus; CC, corpus callosum; CA1, CA1 region of the hippocampus; VTA, ventral tegmental area.
(I) Zoomed-in MSOT images of the substantia nigra and neighboring structures acquired at multiple wavelengths demonstrate wavelength specific optoacoustic absorption. Scale bar, 300 μm.

of newborn rats injected with LPS (Guevara et al., 2013). Yang and colleagues took advantage of a traumatic brain lesion model to monitor the impact and dynamics of a mechanically induced injury in the mouse cortex (Yang et al., 2007). The resulting intracerebral hematoma and lesion were investigated over a 2 week period, with series of images revealing a gradual decrease in the signal intensity and the extent of the hematoma after the insult. Of note, disrupted blood vessels in the lesion area not visible in the early days of imaging appeared at later stages and could be mapped over the injured area, suggesting the concrescence of damaged tissue.

Multi-scale optoacoustic interrogation also proved useful for studies of drug-induced models of focal and generalized seizures. In the neocortex of adult rats, for example, bicuculline-induced seizures were localized and mapped using optoacoustic macroscopy, with focal hypersynchrony confirmed by simultaneous EEG reads (Tsytsarev et al., 2013; Zhang et al., 2008). At microscopic resolution, optoacoustic imaging was applied in conjunction with depth-resolved optical coherence tomography to visualize 4-AP-induced cortical hyperactivity and to monitor changes in the microvasculature surrounding seizure foci (Tsytsarev et al., 2013). To determine whether variations in optoacoustic signals at the localized hyperactivity site are solely due to enhanced oxygen consumption by the excited tissue, involve also secondary changes in the vascular response, or possibly both, paired measurements from the artery and vein were undertaken. It was found that in the seizure foci, both vessel types were strongly dilated, which caused an increase in hemoglobin concentrations over the affected tissue. Recently, Gottschalk and colleagues combined multispectral volumetric optoacoustic tomography and EEG to determine the site of origin and propagation of 4-AP-induced hyperactivity (Gottschalk et al., 2017). A new model for functional imaging of seizure models has been developed, which utilized volumetric hemodynamic measurements with EEG recordings and anatomical mapping to define the role of various brain circuits in initiation and propagation of pathological hyperactivity (Figures 6B and 6C). It is interesting to note that both neuronal and vascular responses to seizure in drug-induced epilepsy models were dynamic and varied significantly depending on the behavioral states of experimental animals (Wang et al., 2015).

Neurodegenerative disease research is another rapidly progressing area where intra-vital imaging holds major potential for basic research and translational applications. In Alzheimer's disease (AD) research, for example, over the past decade, there has been a revolution on the part played by neuroimaging, with diagnostic and clinical imaging transforming from an exclusionary role to a central position (Klunk et al., 2004; Raichle, 2015; Williams, 2013). Imaging is helping to address a wide range of important scientific questions concerning the pathophysiology of AD and related dementias, affording novel insights into the initiation and progression of the disease. In both animal models and in humans, deposits of misfolded amyloid β protein (known as amyloid plaques) have been used as one of the key hallmarks for AD, with different imaging methods utilized for their visualization (Figures 6D and 6E). In the APP-PS1 AD mouse model, optoacoustic microscopy proves capable of resolving amyloid plaques through a cranial opening (Hu et al., 2009b) (Figure 6F). Although in terms of resolution and imaging depth these results were equivalent with those reported earlier with *in vivo* two-photon microscopy (Hefendehl et al., 2011; Meyer-Luehmann et al., 2008; Ovsepian et al., 2017), the proof of principle presented by this report stimulates future implementation of volumetric modalities of optoacoustic imaging for whole-brain studies in animal models of AD. Progress in developing NIR contrast agents (e.g., AOI-987, DANIR-2) selectively labeling amyloid fibrils *in vivo* (Cui, 2014; Cui et al., 2014; Fu et al., 2016; Hintersteiner et al., 2005; Tong et al., 2015) could be of major benefit for advancing this line of research. Sensing endogenous chromophores, such as neuromelanin, neuro-ferritin, and lipofuscin, enriched in selected brain structures could also be useful for future optoacoustic studies of neurodegenerative diseases. Loss of neuromelanin-rich dopaminergic neuron in the substantia nigra and ventral tegmental nucleus, for instance, could be utilized as a reliable biomarker for detection and monitoring the onset and progression Parkinson's disease (PD), the second most prevalent neurodegenerative disease (Figure 6G). Using MSOT of a mouse brain *ex vivo*, midbrain dopaminergic nuclei enriched with neuromelanin have been visualized recently in our pilot studies (I.O., S.V.O., and V.N., unpublished data) (Figures 6H and 6I). Taken as a whole, these developments suggest several new applications for optoacoustic imaging in neurodegenerative disease research, with potentials for sensing cellular and molecular events affecting deep structures such as the basal ganglia, midbrain, and hindbrain nuclei, which reside beyond the reach of other high-resolution optical neuroimaging modalities.

## Outstanding Challenges and Potential Improvements

The exciting research and translational capabilities of optoacoustic imaging come with several major technical and analytical challenges. Sensing and accurate quantification of contrasts in deep tissue remain an area of intense research and development, especially important for multi-spectral optoacoustic imaging (Cox et al., 2009; Cox and Beard, 2009). This is primarily due to the fact that raw optoacoustic measurements do not represent pure absorption spectra but are biased with wavelength- and position-dependent light fluence, resulting in the so-called spectral coloring (Lutzweiler and Razansky, 2013; Tzoumas et al., 2014). To improve the quality of raw optoacoustic data, advanced dyes or signaling compounds with higher molar extinction coefficient and sharper absorption peak are currently under development. These should maximize the light absorption by the chromophores and facilitate their unambiguous spectral decomposition even at low concentrations. Careful selection of contrast agents with absorption peak within the first NIR window (620–950 nm) should maximize the penetration depth of imaging while keeping low the light absorption by endogenous chromophores. Finally, chromophores with improved photostability and low quantum yield are much sought in order to maintain consistent spectral readouts and to maximize the non-radiative decay, enhancing the optoacoustic signal (Weber et al., 2016). These improvements should enhance the SNR and lower the impact of light fluence, which depends on the optical properties and light distribution in the entire sample

(Deán-Ben et al., 2015; Tzoumas et al., 2016). Due to the general complexity of the light transport phenomenon within the matter, which is exaggerated in the brain by complex anatomy and physico-chemical properties of the nervous tissue, spectral irregularities are particularly prominent therein, with solving of the fluence problem holding major promise for quantitative optoacoustic neuroimaging and more accurate measurements of metabolism, neural circuit dynamics, and other complex neurobiological processes.

A standard approach used a model of light propagation to establish a relationship between optical properties of the specimen and light fluence followed by an iterative calculation of the spatial distribution of the optical absorption coefficient (Cox et al., 2009, 2012). This, however, typically results in a computationally unstable problem with challenging application to experimental data. Another approach, championed recently by Tzoumas and colleagues, models spectral shapes of fluence by a linear combination of base pre-computed spectra, termed eigenspectra (Tzoumas et al., 2016). By using information from several spatially distributed locations and appropriate constraints on model parameters, the effects of light fluence on the relative concentrations of $HbO_2$ and Hb could be excluded, leading to more precise $sO_2$ estimations. The disadvantage of such methodology is, however, the assumption that two hemoglobin variants (Hb and $HbO_2$) are the only absorbers in the tissue, which is far from the reality in case of the brain imaging. Furthermore, the method relies on experimentally defined mean optical properties of the sample under investigation, which is known to vary greatly between different tissue types (Jacques, 2013). A somewhat simpler derivative of the spectral decomposition problem is detection of exogenous agent distribution and dynamics. Here, rather than quantifying the concentrations of all (or the most prominent) absorbers, a binary problem for determining the presence of a specific absorber (target) within the specimen can be considered. This approach relies on statistical modeling and suppression of spectral signals from tissue background, therefore identifying the contribution of the molecular target of interest, which is assumed to be present in a small fraction of the imaged domain (Tzoumas et al., 2014, 2015). Recently, some improvements have been made to such methods that involve better modeling based on *in vivo* data from nude mice and accounting for higher target sizes (Tzoumas et al., 2016). Although the preliminary results on the detection of simulated targets in the mouse brain were demonstrated, no detailed data analysis and interpretation were performed. Also, it is unclear whether the proposed background model can be reliably applied across multiple mouse strains, given the reported case-by-case differences in optical properties of brain tissue (Jacques, 2013; Obrig and Villringer, 2003). The sensitivity of such methods for applications in optoacoustic imaging with respect to target concentration and depth has not been characterized.

It is important to note that the performance of the aforementioned methods, especially quantification algorithms, depends on several additional data quality metrics. This is why adequate image reconstruction is still a topic of investigation in optoacoustic imaging, and especially in the field of neuroimaging. Typically, more accurate model-based techniques are used in large-scale imaging, while computationally less expensive back-projection algorithms are employed for rapid image rendering in high-resolution imaging (Deán-Ben et al., 2012a, 2012b; Ding et al., 2015; Lutzweiler and Razansky, 2013; Ntziachristos and Weissleder, 2001). Of note, any optoacoustic reconstruction method depends on the estimated value of the speed of sound in the imaged field of view. It is, therefore, recognized that accounting for acoustic heterogeneities improves the image quality, which is especially important for *in vivo* interrogation of the brain, due to the impact of the skull. The information on the speed of sound heterogeneities and skull location can be obtained from co-registered ultrasound and optoacoustic scans (Merčep et al., 2015; Olefir et al., 2016), with the usefulness of combining such multi-modal imaging data for enhancement of the accuracy of measurements demonstrated (Xia et al., 2013c). Recently, the specific effects of the skull on optoacoustic image resolution were studied in considerable detail, with the approximation of the skull using a solid plate proposed (Kneipp et al., 2016; Li et al., 2016). Other reports focused on dispersion of optoacoustic brain imaging signals, based on model parameters, using co-registered optoacoustic and ultrasound measurements (Estrada et al., 2016; Kneipp et al., 2016). Such models could potentially be useful for correcting skull-induced optical and acoustic aberrations.

Light and sound attenuation due to strong absorption and scattering remain a major obstacle for non-invasive optical and optoacoustic brain imaging studies. In *in vivo* neuroimaging studies, both the incident light and emitted acoustic signal pass through the skull, which in larger animals can reach several millimeters thickness. As a result, the skull strongly scatters and attenuates the light, limiting effective illumination of the brain and collection of acoustic signals. The strong attenuation effects caused by the skull are mostly due to high scattering (Firbank et al., 1993; Nie et al., 2012). Optical clearing of the skull was considered for partially overcoming the scattering problem in the field of two-photon microscopy in small animals (Guo et al., 2014; Wang et al., 2012), also considered for improving the penetration depth with optoacoustic imaging (Yao and Wang, 2014). Yang and colleagues recently presented a clearing method that not only improves imaging depth, but also enhances acoustic transmittance of the skull, partly negating its adverse effects on ultrasound signals (Yang et al., 2016). Enhancing light delivery using titanium-coated photon recycler (Nie et al., 2012; Petrov et al., 2012) has also been considered for improving the transcranial illumination and deeper penetration. Although, in an *ex vivo* experiment with a canine brain covered by a human skull, this approach improved the signal-to-noise ratio 2.4 times (Nie et al., 2012), its utility for intra-vital optoacoustic imaging remains to be shown. Finally, image quality could also benefit from the careful selection of acoustic transducers. Because high frequencies are attenuated faster, the bulk of the optoacoustic signal passed through a human skull resides at frequencies lower than 1 MHz and should be maximally sampled with detection transducers that best match the optoacoustic signal bandwidth. Careful consideration of these and other outstanding issues and taking precautionary measures should improve the illumination and further enhance the real-time volumetric imaging of the structure and functions of healthy and diseased brain using optoacoustic methods.

## Closing Remarks

Optoacoustic imaging is the youngest and arguably one of the most rapidly advancing modality of biomedical observation. As a cutting-edge technology that enables sensing and quantitative interpretation of the characteristics of light-induced acoustic signals in the brain, optoacoustic neuroimaging has reached a degree of maturity, which now permits structural, functional, and molecular interrogation of the entire brain in small animal models in real time at sub-cellular, cellular, and meta-cellular levels. The importance of a multilevel approach in neuroscience has been long recognized as key for the acquisition of in-depth knowledge as to how brain systems work normally as well as how they fail to perform when affected by disease (Marr, 1982; Yuste, 2015). With the central ability to sense and quantify a variety of endo- and exogenous contrast agents, over recent years, optoacoustic neuroimaging has enabled several major breakthroughs in studying the organization and dynamics of the brain in small animal models at multiple scales and dimensions, contracting the gap between neuronal and neural network theories. The wealth of knowledge and information gained with optoacoustic imaging in several fields of biomedical research and especially in neuroimaging will offer rigorously quantitative and robust data on the structure and functions of healthy and diseased brains *in vivo* and inspires confidence toward its advancement as a mainstream and powerful interrogation technique in the foreseeable future.

### ACKNOWLEDGMENTS

The authors' research at the Institute for Biological and Medical Imaging is supported by the German Government and the European Union (Grants VN). D.R.'s grants to be acknowledged: European Research Council Consolidator Grant ERC-2015-CoG-682379, National Institute of Health R21-EY026382-01, Human Frontier Science Program (HFSP) Grant RGY0070/2016, and German-Israeli Foundation (GIF) for Scientific Research and Development 1142-46.10/2011.

### REFERENCES

Aguirre, J., Schwarz, M., Garzorz, N., Omar, M., Buehler, A., Eyerich, K., and Ntziachristos, V. (2017). Precision Assessment of Label-free Psoriasis Biomarkers with Ultra-Broadband Optoacoustic Mesoscopy (Nature Biomedical Engineering).

Attwell, D., and Iadecola, C. (2002). The neural basis of functional brain imaging signals. Trends Neurosci. *25*, 621–625.

Attwell, D., Buchan, A.M., Charpak, S., Lauritzen, M., Macvicar, B.A., and Newman, E.A. (2010). Glial and neuronal control of brain blood flow. Nature *468*, 232–243.

Banks, W.A. (2016). From blood-brain barrier to blood-brain interface: new opportunities for CNS drug delivery. Nat. Rev. Drug Discov. *15*, 275–292.

Bézière, N., and Ntziachristos, V. (2015). Optoacoustic imaging of naphthalocyanine: potential for contrast enhancement and therapy monitoring. J. Nucl. Med. *56*, 323–328.

Boas, D.A., Chen, K., Grebert, D., and Franceschini, M.A. (2004). Improving the diffuse optical imaging spatial resolution of the cerebral hemodynamic response to brain activation in humans. Opt. Lett. *29*, 1506–1508.

Buehler, A., Herzog, E., Razansky, D., and Ntziachristos, V. (2010). Video rate optoacoustic tomography of mouse kidney perfusion. Opt. Lett. *35*, 2475–2477.

Buehler, A., Kacprowicz, M., Taruttis, A., and Ntziachristos, V. (2013). Real-time handheld multispectral optoacoustic imaging. Opt. Lett. *38*, 1404–1406.

Burgold, S., Bittner, T., Dorostkar, M.M., Kieser, D., Fuhrmann, M., Mitteregger, G., Kretzschmar, H., Schmidt, B., and Herms, J. (2011). In vivo multiphoton imaging reveals gradual growth of newborn amyloid plaques over weeks. Acta Neuropathol. *121*, 327–335.

Burton, N.C., Patel, M., Morscher, S., Driessen, W.H., Claussen, J., Beziere, N., Jetzfellner, T., Taruttis, A., Razansky, D., Bednar, B., and Ntziachristos, V. (2013). Multispectral opto-acoustic tomography (MSOT) of the brain and glioblastoma characterization. Neuroimage *65*, 522–528.

Busche, M.A., Eichhoff, G., Adelsberger, H., Abramowski, D., Wiederhold, K.H., Haass, C., Staufenbiel, M., Konnerth, A., and Garaschuk, O. (2008). Clusters of hyperactive neurons near amyloid plaques in a mouse model of Alzheimer's disease. Science *321*, 1686–1689.

Buzsáki, G. (2006). Rhythms of the Brain (Oxford University Press).

Buzsáki, G. (2010). Neural syntax: cell assemblies, synapsembles, and readers. Neuron *68*, 362–385.

Cabeza, R., and Nyberg, L. (1997). Imaging cognition: an empirical review of PET studies with normal subjects. J. Cogn. Neurosci. *9*, 1–26.

Cao, R., Li, J., Ning, B., Sun, N., Wang, T., Zuo, Z., and Hu, S. (2017). Functional and oxygen-metabolic photoacoustic microscopy of the awake mouse brain. Neuroimage *150*, 77–87.

Chekkoury, A., Nunes, A., Gateau, J., Symvoulidis, P., Feuchtinger, A., Beziere, N., Ovsepian, S.V., Walch, A., and Ntziachristos, V. (2016). High-resolution multispectral optoacoustic tomography of the vascularization and constitutive hypoxemia of cancerous tumors. Neoplasia *18*, 459–467.

Chen, X., Leischner, U., Rochefort, N.L., Nelken, I., and Konnerth, A. (2011). Functional mapping of single spines in cortical neurons in vivo. Nature *475*, 501–505.

Compston, A., and Coles, A. (2008). Multiple sclerosis. Lancet *372*, 1502–1517.

Cox, B.T., and Beard, P.C. (2009). Photoacoustic tomography with a single detector in a reverberant cavity. J. Acoust. Soc. Am. *125*, 1426–1436.

Cox, B.T., Arridge, S.R., and Beard, P.C. (2009). Estimating chromophore distributions from multiwavelength photoacoustic images. J. Opt. Soc. Am. A Opt. Image Sci. Vis. *26*, 443–455.

Cox, B., Laufer, J.G., Arridge, S.R., and Beard, P.C. (2012). Quantitative spectroscopic photoacoustic imaging: a review. J. Biomed. Opt. *17*, 061202.

Cui, M. (2014). Past and recent progress of molecular imaging probes for β-amyloid plaques in the brain. Curr. Med. Chem. *21*, 82–112.

Cui, M., Ono, M., Watanabe, H., Kimura, H., Liu, B., and Saji, H. (2014). Smart near-infrared fluorescence probes with donor-acceptor structure for in vivo detection of β-amyloid deposits. J. Am. Chem. Soc. *136*, 3388–3394.

Deán-Ben, X.L., Buehler, A., Ntziachristos, V., and Razansky, D. (2012a). Accurate model-based reconstruction algorithm for three-dimensional optoacoustic tomography. IEEE Trans. Med. Imaging *31*, 1922–1928.

Dean-Ben, X.L., Ntziachristos, V., and Razansky, D. (2012b). Acceleration of optoacoustic model-based reconstruction using angular image discretization. IEEE Trans. Med. Imaging *31*, 1154–1162.

Deán-Ben, X.L., Stiel, A.C., Jiang, Y., Ntziachristos, V., Westmeyer, G.G., and Razansky, D. (2015). Light fluence normalization in turbid tissues via temporally unmixed multispectral optoacoustic tomography. Opt. Lett. *40*, 4691–4694.

Dean-Ben, X.L., Sela, G., Lauri, A., Kneipp, M., Ntziachristos, V., Westmeyer, G.G., Shoham, S., and Razansky, D. (2016). Functional optoacoustic neurotomography for scalable whole-brain monitoring of calcium indicators. Light Sci. Appl. *5*, e16201.

Deliolanis, N.C., Ale, A., Morscher, S., Burton, N.C., Schaefer, K., Radrich, K., Razansky, D., and Ntziachristos, V. (2014). Deep-tissue reporter-gene imaging with fluorescence and optoacoustic tomography: a performance overview. Mol. Imaging Biol. *16*, 652–660.

Deng, C.X. (2010). Targeted drug delivery across the blood-brain barrier using ultrasound technique. Ther. Deliv. *1*, 819–848.

Devor, A., Dunn, A.K., Andermann, M.L., Ulbert, I., Boas, D.A., and Dale, A.M. (2003). Coupling of total hemoglobin concentration, oxygenation, and neural activity in rat somatosensory cortex. Neuron *39*, 353–359.

Dima, A., Burton, N.C., and Ntziachristos, V. (2014). Multispectral optoacoustic tomography at 64, 128, and 256 channels. J. Biomed. Opt. *19*, 36021.

Ding, L., Luís Deán-Ben, X., Lutzweiler, C., Razansky, D., and Ntziachristos, V. (2015). Efficient non-negative constrained model-based inversion in optoacoustic tomography. Phys. Med. Biol. *60*, 6733–6750.

Duncan, J.R., Cock, M.L., Suzuki, K., Scheerlinck, J.P.Y., Harding, R., and Rees, S.M. (2006). Chronic endotoxin exposure causes brain injury in the ovine fetus in the absence of hypoxemia. J. Soc. Gynecol. Investig. *13*, 87–96.

Dunn, A.K., Devor, A., Bolay, H., Andermann, M.L., Moskowitz, M.A., Dale, A.M., and Boas, D.A. (2003). Simultaneous imaging of total cerebral hemoglobin concentration, oxygenation, and blood flow during functional activation. Opt. Lett. *28*, 28–30.

Eggebrecht, A.T., Ferradal, S.L., Robichaux-Viehoever, A., Hassanpour, M.S., Dehghani, H., Snyder, A.Z., Hershey, T., and Culver, J.P. (2014). Mapping distributed brain function and networks with diffuse optical tomography. Nat. Photonics *8*, 448–454.

Estrada, H., Turner, J., Kneipp, M., and Razansky, D. (2014). Real-time optoacoustic brain microscopy with hybrid optical and acoustic resolution. Laser Phys. Lett. Published online February 18, 2014. https://doi.org/10.1088/1612-2011/11/4/045601.

Estrada, H., Rebling, J., Turner, J., and Razansky, D. (2016). Broadband acoustic properties of a murine skull. Phys. Med. Biol. *61*, 1932–1946.

Farahani, K., Sinha, U., Sinha, S., Chiu, L.C., and Lufkin, R.B. (1990). Effect of field strength on susceptibility artifacts in magnetic resonance imaging. Comput. Med. Imaging Graph. *14*, 409–413.

Fernandez, O., Fernandez, V.E., and Guerrero, M. (2015). Demyelinating diseases of the central nervous system. Medicine *11*, 4601–4609.

Filser, S., Ovsepian, S.V., Masana, M., Blazquez-Llorca, L., Brandt Elvang, A., Volbracht, C., Müller, M.B., Jung, C.K., and Herms, J. (2015). Pharmacological inhibition of BACE1 impairs synaptic plasticity and cognitive functions. Biol. Psychiatry *77*, 729–739.

Firbank, M., Hiraoka, M., Essenpreis, M., and Delpy, D.T. (1993). Measurement of the optical properties of the skull in the wavelength range 650-950 nm. Phys. Med. Biol. *38*, 503–510.

Flusberg, B.A., Nimmerjahn, A., Cocker, E.D., Mukamel, E.A., Barretto, R.P., Ko, T.H., Burns, L.D., Jung, J.C., and Schnitzer, M.J. (2008). High-speed, miniaturized fluorescence microscopy in freely moving mice. Nat. Methods *5*, 935–938.

Fox, P.T., Raichle, M.E., Mintun, M.A., and Dence, C. (1988). Nonoxidative glucose consumption during focal physiologic neural activity. Science *241*, 462–464.

Fu, H., Tu, P., Zhao, L., Dai, J., Liu, B., and Cui, M. (2016). Amyloid-β deposits target efficient near-infrared fluorescent probes: synthesis, in vitro evaluation, and in vivo imaging. Anal. Chem. *88*, 1944–1950.

George, J.S. (2010). Casting Light on Neural Function: A Subjective History (Springer).

Ghosh, K.K., Burns, L.D., Cocker, E.D., Nimmerjahn, A., Ziv, Y., Gamal, A.E., and Schnitzer, M.J. (2011). Miniaturized integration of a fluorescence microscope. Nat. Methods *8*, 871–878.

Glatz, J., Deliolanis, N.C., Buehler, A., Razansky, D., and Ntziachristos, V. (2011). Blind source unmixing in multi-spectral optoacoustic tomography. Opt. Express *19*, 3175–3184.

Gottschalk, S., Fehm, T.F., Deán-Ben, X.L., and Razansky, D. (2015). Noninvasive real-time visualization of multiple cerebral hemodynamic parameters in whole mouse brains using five-dimensional optoacoustic tomography. J. Cereb. Blood Flow Metab. *35*, 531–535.

Gottschalk, S., Fehm, T.F., Deán-Ben, X.L., Tsytsarev, V., and Razansky, D. (2017). Correlation between volumetric oxygenation responses and electrophysiology identifies deep thalamocortical activity during epileptic seizures. Neurophotonics *4*, 011007.

Gratton, G., Chiarelli, A.M., and Fabiani, M. (2017). From brain to blood vessels and back: a noninvasive optical imaging approach. Neurophotonics *4*, 031208.

Grienberger, C., and Konnerth, A. (2012). Imaging calcium in neurons. Neuron *73*, 862–885.

Grinvald, A., Lieke, E., Frostig, R.D., Gilbert, C.D., and Wiesel, T.N. (1986). Functional architecture of cortex revealed by optical imaging of intrinsic signals. Nature *324*, 361–364.

Grinvald, A., Shoham, D., Shmuel, A., Glaser, D., Vanzetta, I., Shtoyerman, E., Slovin, H., Wijnbergen, C., and Hildesheim, R. (1999). In Vivo Optical Imaging of Cortical Architecture and Dynamics (Springer Verlag).

Gu, Z., Taschereau, R., Vu, N.T., Wang, H., Prout, D.L., Silverman, R.W., Bai, B., Stout, D.B., Phelps, M.E., and Chatziioannou, A.F. (2013). NEMA NU-4 performance evaluation of PETbox4, a high sensitivity dedicated PET preclinical tomograph. Phys. Med. Biol. *58*, 3791–3814.

Guevara, E., Berti, R., Londono, I., Xie, N., Bellec, P., Lesage, F., and Lodygensky, G.A. (2013). Imaging of an inflammatory injury in the newborn rat brain with photoacoustic tomography. PLoS ONE *8*, e83045.

Gujrati, V., Mishra, A., and Ntziachristos, V. (2017). Molecular imaging probes for multi-spectral optoacoustic tomography. Chem. Commun. (Camb.) *53*, 4653–4672.

Guo, Z.V., Li, N., Huber, D., Ophir, E., Gutnisky, D., Ting, J.T., Feng, G., and Svoboda, K. (2014). Flow of cortical activity underlying a tactile decision in mice. Neuron *81*, 179–194.

Harris, S., Ma, H., Zhao, M., Boorman, L., Zheng, Y., Kennerley, A., Bruyns-Haylett, M., Overton, P.G., Berwick, J., and Schwartz, T.H. (2014). Coupling between gamma-band power and cerebral blood volume during recurrent acute neocortical seizures. Neuroimage *97*, 62–70.

Hawco, C.S., Bagshaw, A.P., Lu, Y., Dubeau, F., and Gotman, J. (2007). BOLD changes occur prior to epileptic spikes seen on scalp EEG. Neuroimage *35*, 1450–1458.

Hebb, D.O. (2002). The Organization of Behavior: A Neuropsychological Theory (L. Erlbaum Associates).

Hefendehl, J.K., Wegenast-Braun, B.M., Liebig, C., Eicke, D., Milford, D., Calhoun, M.E., Kohsaka, S., Eichner, M., and Jucker, M. (2011). Long-term in vivo imaging of β-amyloid plaque appearance and growth in a mouse model of cerebral β-amyloidosis. J. Neurosci. *31*, 624–629.

Helmchen, F., and Denk, W. (2005). Deep tissue two-photon microscopy. Nat. Methods *2*, 932–940.

Herzog, E., Taruttis, A., Beziere, N., Lutich, A.A., Razansky, D., and Ntziachristos, V. (2012). Optical imaging of cancer heterogeneity with multispectral optoacoustic tomography. Radiology *263*, 461–468.

Hillman, E.M. (2007). Optical brain imaging in vivo: techniques and applications from animal to man. J. Biomed. Opt. *12*, 051402.

Hillman, E.M. (2014). Coupling mechanism and significance of the BOLD signal: a status report. Annu. Rev. Neurosci. *37*, 161–181.

Hintersteiner, M., Enz, A., Frey, P., Jaton, A.L., Kinzy, W., Kneuer, R., Neumann, U., Rudin, M., Staufenbiel, M., Stoeckli, M., et al. (2005). In vivo detection of amyloid-beta deposits by near-infrared imaging using an oxazine-derivative probe. Nat. Biotechnol. *23*, 577–583.

Hoeffner, E.G., Mukherji, S.K., Srinivasan, A., and Quint, D.J. (2012). Neuroradiology back to the future: brain imaging. AJNR Am. J. Neuroradiol. *33*, 5–11.

Hoelen, C.G., de Mul, F.F., Pongers, R., and Dekker, A. (1998). Three-dimensional photoacoustic imaging of blood vessels in tissue. Opt. Lett. *23*, 648–650.

Holcman, D., and Yuste, R. (2015). The new nanophysiology: regulation of ionic flow in neuronal subcompartments. Nat. Rev. Neurosci. *16*, 685–692.

Hoyer, C., Gass, N., Weber-Fahr, W., and Sartorius, A. (2014). Advantages and challenges of small animal magnetic resonance imaging as a translational tool. Neuropsychobiology *69*, 187–201.

Hu, S. (2016). Listening to the brain with photoacoustics. IEEExplore. Published online October 7, 2015. https://doi.org/10.1109/JSTQE.2015.2487890.

Hu, S., Maslov, K., Tsytsarev, V., and Wang, L.V. (2009a). Functional transcranial brain imaging by optical-resolution photoacoustic microscopy. J. Biomed. Opt. *14*, 040503.

Hu, S., Yan, P., Maslov, K., Lee, J.M., and Wang, L.V. (2009b). Intravital imaging of amyloid plaques in a transgenic mouse model using optical-resolution photoacoustic microscopy. Opt. Lett. *34*, 3899–3901.

Hu, S., Gonzales, E., Soetikno, B., Gong, E., Yan, P., Maslov, K., Lee, J.M., and Wang, L.V. (2011). Optical-resolution photoacoustic microscopy of ischemic stroke. Proc. SPIE *7899*, 789906.

Ibaraki, M., Shimosegawa, E., Miura, S., Takahashi, K., Ito, H., Kanno, I., and Hatazawa, J. (2004). PET measurements of CBF, OEF, and CMRO2 without arterial sampling in hyperacute ischemic stroke: method and error analysis. Ann. Nucl. Med. *18*, 35–44.

Jacques, S.L. (2013). Optical properties of biological tissues: a review. Phys. Med. Biol. *58*, R37–R61.

Jain, K.K. (2012). Nanobiotechnology-based strategies for crossing the blood-brain barrier. Nanomedicine (Lond.) *7*, 1225–1233.

James, M.L., and Gambhir, S.S. (2012). A molecular imaging primer: modalities, imaging agents, and applications. Physiol. Rev. *92*, 897–965.

Katona, G., Szalay, G., Maák, P., Kaszás, A., Veress, M., Hillier, D., Chiovini, B., Vizi, E.S., Roska, B., and Rózsa, B. (2012). Fast two-photon in vivo imaging with three-dimensional random-access scanning in large tissue volumes. Nat. Methods *9*, 201–208.

Kennan, R.P., Kim, D., Maki, A., Koizumi, H., and Constable, R.T. (2002). Non-invasive assessment of language lateralization by transcranial near infrared optical topography and functional MRI. Hum. Brain Mapp. *16*, 183–189.

Kircher, M.F., de la Zerda, A., Jokerst, J.V., Zavaleta, C.L., Kempen, P.J., Mittra, E., Pitter, K., Huang, R., Campos, C., Habte, F., et al. (2012). A brain tumor molecular imaging strategy using a new triple-modality MRI-photoacoustic-Raman nanoparticle. Nat. Med. *18*, 829–834.

Klunk, W.E., Engler, H., Nordberg, A., Wang, Y., Blomqvist, G., Holt, D.P., Bergström, M., Savitcheva, I., Huang, G.F., Estrada, S., et al. (2004). Imaging brain amyloid in Alzheimer's disease with Pittsburgh Compound-B. Ann. Neurol. *55*, 306–319.

Kneipp, M., Turner, J., Hambauer, S., Krieg, S.M., Lehmberg, J., Lindauer, U., and Razansky, D. (2014). Functional real-time optoacoustic imaging of middle cerebral artery occlusion in mice. PLoS ONE *9*, e96118.

Kneipp, M., Turner, J., Estrada, H., Rebling, J., Shoham, S., and Razansky, D. (2016). Effects of the murine skull in optoacoustic brain microscopy. J. Biophotonics *9*, 117–123.

Koch, C., and Reid, R.C. (2012). Neuroscience: observatories of the mind. Nature *483*, 397–398.

Kruger, R.A., Liu, P., Fang, Y.R., and Appledorn, C.R. (1995). Photoacoustic ultrasound (PAUS)–reconstruction tomography. Med. Phys. *22*, 1605–1609.

Laufer, J., Delpy, D., Elwell, C., and Beard, P. (2007). Quantitative spatially resolved measurement of tissue chromophore concentrations using photoacoustic spectroscopy: application to the measurement of blood oxygenation and haemoglobin concentration. Phys. Med. Biol. *52*, 141–168.

Laufer, J., Zhang, E., Raivich, G., and Beard, P. (2009). Three-dimensional noninvasive imaging of the vasculature in the mouse brain using a high resolution photoacoustic scanner. Appl. Opt. *48*, D299–D306.

Laufer, J., Johnson, P., Zhang, E., Treeby, B., Cox, B., Pedley, B., and Beard, P. (2012). In vivo preclinical photoacoustic imaging of tumor vasculature development and therapy. J. Biomed. Opt. *17*, 056016.

Li, M.L., Oh, J.T., Xie, X.Y., Ku, G., Wang, W., Li, C., Lungu, G., Stoica, G., and Wang, L.V. (2008). Simultaneous molecular and hypoxia imaging of brain tumors in vivo using spectroscopic photoacoustic tomography. IEEExplore *96*, 481–489.

Li, C., Aguirre, A., Gamelin, J., Maurudis, A., Zhu, Q., and Wang, L.V. (2010). Real-time photoacoustic tomography of cortical hemodynamics in small animals. J. Biomed. Opt. *15*, 010509.

Li, L., Xia, J., Li, G., Garcia-Uribe, A., Sheng, Q.W., Anastasio, M.A., and Wang, L.V. (2016). Label-free photoacoustic tomography of whole mouse brain structures ex vivo. Neurophotonics *3*, 035001.

Liao, L.D., Lin, C.T., Shih, Y.Y., Duong, T.Q., Lai, H.Y., Wang, P.H., Wu, R., Tsang, S., Chang, J.Y., Li, M.L., and Chen, Y.Y. (2012a). Transcranial imaging of functional cerebral hemodynamic changes in single blood vessels using in vivo photoacoustic microscopy. J. Cereb. Blood Flow Metab. *32*, 938–951.

Liao, L.D., Lin, C.T., Shih, Y.Y., Lai, H.Y., Zhao, W.T., Duong, T.Q., Chang, J.Y., Chen, Y.Y., and Li, M.L. (2012b). Investigation of the cerebral hemodynamic response function in single blood vessels by functional photoacoustic microscopy. J. Biomed. Opt. *17*, 061210.

Liao, L.D., Li, M.L., Lai, H.Y., Chen, Y.Y., and Thakor, N.V. (2013a). Study of neurovascular coupling functions for transient focal cerebral ischemia in rats using electrocorticography functional photoacoustic microscopy (ECoG-fPAM). In Proceedings of the 2013 Annual International Conference of the IEEE Engineering in Medicine and Biology Society (IEEE Engineering in Medicine and Biology Society), pp. 1799–1802.

Liao, L.D., Tsytsarev, V., Delgado-Martínez, I., Li, M.L., Erzurumlu, R., Vipin, A., Orellana, J., Lin, Y.R., Lai, H.Y., Chen, Y.Y., and Thakor, N.V. (2013b). Neurovascular coupling: in vivo optical techniques for functional brain imaging. Biomed. Eng. Online *12*, 38.

Lin, L., Xia, J., Wong, T.T.W., Li, L., and Wang, L.V. (2015). In vivo deep brain imaging of rats using oral-cavity illuminated photoacoustic computed tomography. J. Biomed. Opt. *20*, 016019.

Logothetis, N.K. (2008). What we can do and what we cannot do with fMRI. Nature *453*, 869–878.

Lozano, N., Al-Jamal, W.T., Taruttis, A., Beziere, N., Burton, N.C., Van den Bossche, J., Mazza, M., Herzog, E., Ntziachristos, V., and Kostarelos, K. (2012). Liposome-gold nanorod hybrids for high-resolution visualization deep in tissues. J. Am. Chem. Soc. *134*, 13256–13258.

Lutzweiler, C., and Razansky, D. (2013). Optoacoustic imaging and tomography: reconstruction approaches and outstanding challenges in image performance and quantification. Sensors (Basel) *13*, 7345–7384.

Lutzweiler, C., Meier, R., Rummeny, E., Ntziachristos, V., and Razansky, D. (2014). Real-time optoacoustic tomography of indocyanine green perfusion and oxygenation parameters in human finger vasculature. Opt. Lett. *39*, 4061–4064.

Ma, H., Geneslaw, A., Zhao, M., Suh, M., Perry, C., and Schwartz, T.H. (2009). The importance of latency in the focality of perfusion and oxygenation changes associated with triggered afterdischarges in human cortex. J. Cereb. Blood Flow Metab. *29*, 1003–1014.

Ma, R., Distel, M., Deán-Ben, X.L., Ntziachristos, V., and Razansky, D. (2012a). Non-invasive whole-body imaging of adult zebrafish with optoacoustic tomography. Phys. Med. Biol. *57*, 7227–7237.

Ma, R., Söntges, S., Shoham, S., Ntziachristos, V., and Razansky, D. (2012b). Fast scanning coaxial optoacoustic microscopy. Biomed. Opt. Express *3*, 1724–1731.

Malonek, D., and Grinvald, A. (1996). Interactions between electrical activity and cortical microcirculation revealed by imaging spectroscopy: implications for functional brain mapping. Science *272*, 551–554.

Malonek, D., Dirnagl, U., Lindauer, U., Yamada, K., Kanno, I., and Grinvald, A. (1997). Vascular imprints of neuronal activity: relationships between the dynamics of cortical blood flow, oxygenation, and volume changes following sensory stimulation. Proc. Natl. Acad. Sci. USA *94*, 14826–14831.

Margrie, T.W., Brecht, M., and Sakmann, B. (2002). In vivo, low-resistance, whole-cell recordings from neurons in the anaesthetized and awake mammalian brain. Pflugers Arch. *444*, 491–498.

Mari, J.M., Westb, S., Bearda, P.C., and Desjardinsa, A.E. (2014). Multispectral photoacoustic imaging of nerves with a clinical ultrasound system. Proc. SPIE *8943*, 89430W.

Marr, D. (1982). Vision: A Computational Investigation into the Human Representation and Processing of Visual Information (W.H. Freeman).

Martin, C., Martindale, J., Berwick, J., and Mayhew, J. (2006). Investigating neural-hemodynamic coupling and the hemodynamic response function in the awake rat. Neuroimage *32*, 33–48.

Matthews, T.P., Zhang, C., Yao, D.K., Maslov, K., and Wang, L.V. (2014). Label-free photoacoustic microscopy of peripheral nerves. J. Biomed. Opt. *19*, 16004.

Merčep, E., Burton, N.C., Claussen, J., and Razansky, D. (2015). Whole-body live mouse imaging by hybrid reflection-mode ultrasound and optoacoustic tomography. Opt. Lett. *40*, 4643–4646.

Mesulam, M.M. (1998). From sensation to cognition. Brain *121*, 1013–1052.

Meyer-Luehmann, M., Spires-Jones, T.L., Prada, C., Garcia-Alloza, M., de Calignon, A., Rozkalne, A., Koenigsknecht-Talboo, J., Holtzman, D.M., Bacskai, B.J., and Hyman, B.T. (2008). Rapid appearance and local toxicity of amyloid-beta plaques in a mouse model of Alzheimer's disease. Nature *451*, 720–724.

Mountcastle, V.B. (1997). The columnar organization of the neocortex. Brain *120*, 701–722.

Nasiriavanaki, M., Xia, J., Wan, H., Bauer, A.Q., Culver, J.P., and Wang, L.V. (2014). High-resolution photoacoustic tomography of resting-state functional connectivity in the mouse brain. Proc. Natl. Acad. Sci. USA *111*, 21–26.

Needles, A., Heinmiller, A., Sun, J., Theodoropoulos, C., Bates, D., Hirson, D., Yin, M., and Foster, F.S. (2013). Development and initial application of a fully integrated photoacoustic micro-ultrasound system. IEEE Trans. Ultrason. Ferroelectr. Freq. Control *60*, 888–897.

Nie, L., Cai, X., Maslov, K., Garcia-Uribe, A., Anastasio, M.A., and Wang, L.V. (2012). Photoacoustic tomography through a whole adult human skull with a photon recycler. J. Biomed. Opt. *17*, 110506.

Ntziachristos, V. (2010). Going deeper than microscopy: the optical imaging frontier in biology. Nat. Methods *7*, 603–614.

Ntziachristos, V., and Razansky, D. (2010). Molecular imaging by means of multispectral optoacoustic tomography (MSOT). Chem. Rev. *110*, 2783–2794.

Ntziachristos, V., and Weissleder, R. (2001). Experimental three-dimensional fluorescence reconstruction of diffuse media by use of a normalized Born approximation. Opt. Lett. *26*, 893–895.

Ntziachristos, V., Ma, X.H., Yodh, A.G., and Chance, B. (1999). Multichannel photon counting instrument for spatially resolved near infrared spectroscopy. Rev. Sci. Instrum. *70*, 193–201.

Ntziachristos, V., Ripoll, J., Wang, L.V., and Weissleder, R. (2005). Looking and listening to light: the evolution of whole-body photonic imaging. Nat. Biotechnol. *23*, 313–320.

O'Leary, V.B., Ovsepian, S.V., Bodeker, M., and Dolly, J.O. (2013). Improved lentiviral transduction of ALS motoneurons in vivo via dual targeting. Mol. Pharm. *10*, 4195–4206.

Obrig, H., and Villringer, A. (2003). Beyond the visible–imaging the human brain with light. J. Cereb. Blood Flow Metab. *23*, 1–18.

Ogawa, S., Lee, T.M., Kay, A.R., and Tank, D.W. (1990). Brain magnetic resonance imaging with contrast dependent on blood oxygenation. Proc. Natl. Acad. Sci. USA *87*, 9868–9872.

Olefir, I., Mercep, E., Burton, N.C., Ovsepian, S.V., and Ntziachristos, V. (2016). Hybrid multispectral optoacoustic and ultrasound tomography for morphological and physiological brain imaging. J. Biomed. Opt. *21*, 86005.

Omar, M., Soliman, D., Gateau, J., and Ntziachristos, V. (2014). Ultrawideband reflection-mode optoacoustic mesoscopy. Opt. Lett. *39*, 3911–3914.

Oraevsky, A., Andreev, V., Karabutov, A., Fleming, D., Gatalica, Z., Singh, H., and Esenaliev, R. (1999). Laser optoacoustic imaging of the breast: detection of cancer angiogenesis. Proc. SPIE *3597*, 352–363.

Osharina, V., Ponchel, E., Aarabi, A., Grebe, R., and Wallois, F. (2010). Local haemodynamic changes preceding interictal spikes: a simultaneous electrocorticography (ECoG) and near-infrared spectroscopy (NIRS) analysis in rats. Neuroimage *50*, 600–607.

Ouzounov, D.G., Wang, T., Wang, M., Feng, D.D., Horton, N.G., Cruz-Hernández, J.C., Cheng, Y.T., Reimer, J., Tolias, A.S., Nishimura, N., and Xu, C. (2017). In vivo three-photon imaging of activity of GCaMP6-labeled neurons deep in intact mouse brain. Nat. Methods *14*, 388–390.

Ovsepian, S.V., Bodeker, M., O'Leary, V.B., Lawrence, G.W., and Oliver Dolly, J. (2015). Internalization and retrograde axonal trafficking of tetanus toxin in motor neurons and trans-synaptic propagation at central synapses exceed those of its C-terminal-binding fragments. Brain Struct. Funct. *220*, 1825–1838.

Ovsepian, S.V., O'Leary, V.B., Ntziachristos, V., and Dolly, J.O. (2016). Circumventing brain barriers: nanovehicles for retroaxonal therapeutic delivery. Trends Mol. Med. *22*, 983–993.

Ovsepian, S.V., Blazquez-Llorca, L., Freitag, S.V., Rodrigues, E.F., and Herms, J. (2017). Ambient glutamate promotes paroxysmal hyperactivity in cortical pyramidal neurons at amyloid plaques via presynaptic mGluR1 receptors. Cereb. Cortex *27*, 4733–4749.

Paproski, R.J., Heinmiller, A., Wachowicz, K., and Zemp, R.J. (2014). Multi-wavelength photoacoustic imaging of inducible tyrosinase reporter gene expression in xenograft tumors. Sci. Rep. *4*, 5329.

Peterka, D.S., Takahashi, H., and Yuste, R. (2011). Imaging voltage in neurons. Neuron *69*, 9–21.

Petrov, I.Y., Petrov, Y., Prough, D.S., Cicenaite, I., Deyo, D.J., and Esenaliev, R.O. (2012). Optoacoustic monitoring of cerebral venous blood oxygenation though intact scalp in large animals. Opt. Express *20*, 4159–4167.

Posner, M.I., and Raichle, M.E. (1998). The neuroimaging of human brain function. Proc. Natl. Acad. Sci. USA *95*, 763–764.

Raichle, M.E. (1998). Behind the scenes of functional brain imaging: a historical and physiological perspective. Proc. Natl. Acad. Sci. USA *95*, 765–772.

Raichle, M.E. (2015). The brain's default mode network. Annu. Rev. Neurosci. *38*, 433–447.

Razansky, D., Vinegoni, C., and Ntziachristos, V. (2007). Multispectral photoacoustic imaging of fluorochromes in small animals. Opt. Lett. *32*, 2891–2893.

Razansky, D., Baeten, J., and Ntziachristos, V. (2009a). Sensitivity of molecular target detection by multispectral optoacoustic tomography (MSOT). Med. Phys. *36*, 939–945.

Razansky, D., Distel, M., Vinegoni, C., Ma, R., Perrimon, N., Koster, R.W., and Ntziachristos, V. (2009b). Multispectral opto-acoustic tomography of deep-seated fluorescent proteins in vivo. Nat. Photonics *3*, 412–417.

Razansky, D., Buehler, A., and Ntziachristos, V. (2011). Volumetric real-time multispectral optoacoustic tomography of biomarkers. Nat. Protoc. *6*, 1121–1129.

Razansky, D., Harlaar, N.J., Hillebrands, J.L., Taruttis, A., Herzog, E., Zeebregts, C.J., van Dam, G.M., and Ntziachristos, V. (2012). Multispectral optoacoustic tomography of matrix metalloproteinase activity in vulnerable human carotid plaques. Mol. Imaging Biol. *14*, 277–285.

Rivera, D.R., Brown, C.M., Ouzounov, D.G., Pavlova, I., Kobat, D., Webb, W.W., and Xu, C. (2011). Compact and flexible raster scanning multiphoton endoscope capable of imaging unstained tissue. Proc. Natl. Acad. Sci. USA *108*, 17598–17603.

Rosencwaig, A. (1973). Photoacoustic spectroscopy of biological materials. Science *181*, 657–658.

Rosencwaig, A. (1982). Potential clinical applications of photoacoustics. Clin. Chem. *28*, 1878–1881.

Roy, C.S., and Sherrington, C.S. (1890). On the regulation of the blood-supply of the brain. J. Physiol. *11*, 85–158.17.

Ruan, Q., Xi, L., Boye, S.L., Han, S., Chen, Z.J., Hauswirth, W.W., Lewin, A.S., Boulton, M.E., Law, B.K., Jiang, W.G., et al. (2013). Development of an anti-angiogenic therapeutic model combining scAAV2-delivered siRNAs and noninvasive photoacoustic imaging of tumor vasculature development. Cancer Lett. *332*, 120–129.

Schwarz, M., Soliman, D., Omar, M., Buehler, A., Ovsepian, S.V., Aguirre, J., and Ntziachristos, V. (2017). Optoacoustic dermoscopy of the human skin: tuning excitation energy for optimal detection bandwidth with fast and deep imaging in vivo. IEEE Trans. Med. Imaging *36*, 1287–1296.

Siegel, G., Albers, R.W., Brady, S., and Price, D. (2006). Basic Neurochemistry: Molecular, Cellular and Medical Aspects, Seventh Edition (Elsevier Academic Press).

Sim, N., Gottschalk, S., Pal, R., Delbianco, M., Degtyaruk, O., Razansky, D., Westmeyer, G.G., Ntziachristos, V., Parker, D., and Mishra, A. (2015). Wavelength-dependent optoacoustic imaging probes for NMDA receptor visualisation. Chem. Commun. (Camb.) *51*, 15149–15152.

Sofroniew, N.J., Flickinger, D., King, J., and Svoboda, K. (2016). A large field of view two-photon mesoscope with subcellular resolution for in vivo imaging. eLife *5*, 5.

Soliman, D., Tserevelakis, G.J., Omar, M., and Ntziachristos, V. (2015). Combining microscopy with mesoscopy using optical and optoacoustic label-free modes. Sci. Rep. *5*, 12902.

Song, K.H., and Wang, L.V. (2007). Deep reflection-mode photoacoustic imaging of biological tissue. J. Biomed. Opt. *12*, 060503.

Staley, J., Grogan, P., Samadi, A.K., Cui, H., Cohen, M.S., and Yang, X. (2010). Growth of melanoma brain tumors monitored by photoacoustic microscopy. J. Biomed. Opt. *15*, 040510.

Stein, E.W., Maslov, K., and Wang, L.V. (2009a). Noninvasive, in vivo imaging of blood-oxygenation dynamics within the mouse brain using photoacoustic microscopy. J. Biomed. Opt. *14*, 020502.

Stein, E.W., Maslov, K., and Wang, L.V. (2009b). Noninvasive, in vivo imaging of the mouse brain using photoacoustic microscopy. J. Appl. Phys. *105*, 102027.

Stritzker, J., Kirscher, L., Scadeng, M., Deliolanis, N.C., Morscher, S., Symvoulidis, P., Schaefer, K., Zhang, Q., Buckel, L., Hess, M., et al. (2013a). Vaccinia virus-mediated melanin production allows MR and optoacoustic deep tissue imaging and laser-induced thermotherapy of cancer. Proc. Natl. Acad. Sci. USA *110*, 3316–3320.

Stritzker, J., Kirscher, L., Scadeng, M., Deliolanis, N.C., Morscher, S., Symvoulidis, P., Schaefer, K., Zhang, Q., Hess, M., Buckel, L., et al. (2013b). Melanin production by oncolytic vaccinia virus strains allows MR and optoacoustic deep-tissue imaging and laser-induced thermotherapy of cancer. J. Nucl. Med. *54*, 23–24.

Svoboda, K., and Yasuda, R. (2006). Principles of two-photon excitation microscopy and its applications to neuroscience. Neuron *50*, 823–839.

Szabo, V., Ventalon, C., De Sars, V., Bradley, J., and Emiliani, V. (2014). Spatially selective holographic photoactivation and functional fluorescence imaging in freely behaving mice with a fiberscope. Neuron *84*, 1157–1169.

Tang, J., Xi, L., Zhou, J., Huang, H., Zhang, T., Carney, P.R., and Jiang, H. (2015). Noninvasive high-speed photoacoustic tomography of cerebral hemodynamics in awake-moving rats. J. Cereb. Blood Flow Metab. *35*, 1224–1232.

Tang, J., Coleman, J.E., Dai, X., and Jiang, H. (2016). Wearable 3-D photoacoustic tomography for functional brain imaging in behaving rats. Sci. Rep. *6*, 25470.

Taruttis, A., and Ntziachristos, V. (2015). Advances in real-time multispectral optoacoustic imaging and its applications. Nat. Photonics *9*, 219–227.

Taruttis, A., Wildgruber, M., Kosanke, K., Beziere, N., Licha, K., Haag, R., Aichler, M., Walch, A., Rummeny, E., and Ntziachristos, V. (2012). Multispectral optoacoustic tomography of myocardial infarction. Photoacoustics *1*, 3–8.

Taruttis, A., van Dam, G.M., and Ntziachristos, V. (2015). Mesoscopic and macroscopic optoacoustic imaging of cancer. Cancer Res. *75*, 1548–1559.

Tenney, J.R., Duong, T.Q., King, J.A., Ludwig, R., and Ferris, C.F. (2003). Corticothalamic modulation during absence seizures in rats: a functional MRI assessment. Epilepsia *44*, 1133–1140.

Tong, H., Lou, K., and Wang, W. (2015). Near-infrared fluorescent probes for imaging of amyloid plaques in Alzheimer's disease. Acta Pharm. Sin. B *5*, 25–33.

Tsytsarev, V., Maslov, K.I., Yao, J., Parameswar, A.R., Demchenko, A.V., and Wang, L.V. (2012). In vivo imaging of epileptic activity using 2-NBDG, a fluorescent deoxyglucose analog. J. Neurosci. Methods *203*, 136–140.

Tsytsarev, V., Rao, B., Maslov, K.I., Li, L., and Wang, L.V. (2013). Photoacoustic and optical coherence tomography of epilepsy with high temporal and spatial resolution and dual optical contrasts. J. Neurosci. Methods *216*, 142–145.

Tzoumas, S., Deliolanis, N., Morscher, S., and Ntziachristos, V. (2014). Unmixing molecular agents from absorbing tissue in multispectral optoacoustic tomography. IEEE Trans. Med. Imaging *33*, 48–60.

Tzoumas, S., Nunes, A., Deliolanis, N.C., and Ntziachristos, V. (2015). Effects of multispectral excitation on the sensitivity of molecular optoacoustic imaging. J. Biophotonics *8*, 629–637.

Tzoumas, S., Nunes, A., Olefir, I., Stangl, S., Symvoulidis, P., Glasl, S., Bayer, C., Multhoff, G., and Ntziachristos, V. (2016). Eigenspectra optoacoustic tomography achieves quantitative blood oxygenation imaging deep in tissues. Nat. Commun. *7*, 12121.

Wang, L.V., and Hu, S. (2012). Photoacoustic tomography: in vivo imaging from organelles to organs. Science *335*, 1458–1462.

Wang, X., Pang, Y., Ku, G., Xie, X., Stoica, G., and Wang, L.V. (2003). Noninvasive laser-induced photoacoustic tomography for structural and functional in vivo imaging of the brain. Nat. Biotechnol. *21*, 803–806.

Wang, M., Etu, J., and Joshi, S. (2007). Enhanced disruption of the blood brain barrier by intracarotid mannitol injection during transient cerebral hypoperfusion in rabbits. J. Neurosurg. Anesthesiol. *19*, 249–256.

Wang, J., Zhang, Y., Xu, T.H., Luo, Q.M., and Zhu, D. (2012). An innovative transparent cranial window based on skull optical clearing. Laser Phys. Lett. *9*, 469–473.

Wang, L., Maslov, K., and Wang, L.V. (2013). Single-cell label-free photoacoustic flowoxigraphy in vivo. Proc. Natl. Acad. Sci. USA *110*, 5759–5764.

Wang, B., Zhou, J., Carney, P., and Jiang, H. (2015). A novel detachable head-mounted device for simultaneous EEG and photoacoustic monitoring of epilepsy in freely moving rats. Neurosci. Res. *91*, 57–62.

Weber, J., Beard, P.C., and Bohndiek, S.E. (2016). Contrast agents for molecular photoacoustic imaging. Nat. Methods *13*, 639–650.

Weissleder, R., and Ntziachristos, V. (2003). Shedding light onto live molecular targets. Nat. Med. *9*, 123–128.

Weissleder, R., and Pittet, M.J. (2008). Imaging in the era of molecular oncology. Nature *452*, 580–589.

White, B.R., Bauer, A.Q., Snyder, A.Z., Schlaggar, B.L., Lee, J.M., and Culver, J.P. (2011). Imaging of functional connectivity in the mouse brain. PLoS ONE *6*, e16322.

Williams, S.C. (2013). Alzheimer's disease: mapping the brain's decline. Nature *502*, S84–S85.

Wilson, K.E., Wang, T.Y., and Willmann, J.K. (2013). Acoustic and photoacoustic molecular imaging of cancer. J. Nucl. Med. *54*, 1851–1854.

Winkler, A.M., Maslov, K., and Wang, L.V. (2013). Noise-equivalent sensitivity of photoacoustics. J. Biomed. Opt. *18*, 097003.

Wu, W., Wang, P., Cheng, J.X., and Xu, X.M. (2014). Assessment of white matter loss using bond-selective photoacoustic imaging in a rat model of contusive spinal cord injury. J. Neurotrauma *31*, 1998–2002.

Xia, J., Danielli, A., Liu, Y., Wang, L., Maslov, K., and Wang, L.V. (2013a). Calibration-free quantification of absolute oxygen saturation based on the dynamics of photoacoustic signals. Opt. Lett. *38*, 2800–2803.

Xia, J., Li, G., Wang, L., Nasiriavanaki, M., Maslov, K., Engelbach, J.A., Garbow, J.R., and Wang, L.V. (2013b). Wide-field two-dimensional multifocal optical-resolution photoacoustic-computed microscopy. Opt. Lett. *38*, 5236–5239.

Xia, Y., Yao, R., Deng, X., Liu, Y., Wang, S., and Ma, T. (2013c). Assessment of hybrid rotation-translation scan schemes for in vivo animal SPECT imaging. Phys. Med. Biol. *58*, 965–983.

Xing, W., Wang, L., Maslov, K., and Wang, L.V. (2013). Integrated optical- and acoustic-resolution photoacoustic microscopy based on an optical fiber bundle. Opt. Lett. *38*, 52–54.

Xu, Z., Zhu, Q., and Wang, L.V. (2011). In vivo photoacoustic tomography of mouse cerebral edema induced by cold injury. J. Biomed. Opt. *16*, 066020.

Yang, X., and Wang, L.V. (2008). Monkey brain cortex imaging by photoacoustic tomography. J. Biomed. Opt. *13*, 044009.

Yang, W., and Yuste, R. (2017). In vivo imaging of neural activity. Nat. Methods *14*, 349–359.

Yang, X., Hyder, F., and Shulman, R.G. (1997). Functional MRI BOLD signal coincides with electrical activity in the rat whisker barrels. Magn. Reson. Med. *38*, 874–877.

Yang, S.H., Xing, D., Lao, Y.Q., Yang, D.W., Zeng, L.M., Xiang, L.Z., and Chen, W.R. (2007). Noninvasive monitoring of traumatic brain injury and post-traumatic rehabilitation with laser-induced photoacoustic imaging. Appl. Phys. Lett. *90*, 243902.

Yang, X., Zhang, Y., Zhao, K., Zhao, Y., Liu, Y., Gong, H., Luo, Q., and Zhu, D. (2016). Skull optical clearing solution for enhancing ultrasonic and photoacoustic imaging. IEEE Trans. Med. Imaging *35*, 1903–1906.

Yao, J., and Wang, L.V. (2014). Photoacoustic brain imaging: from microscopic to macroscopic scales. Neurophotonics *1*, 1.

Yao, J., Xia, J., Maslov, K.I., Nasiriavanaki, M., Tsytsarev, V., Demchenko, A.V., and Wang, L.V. (2013). Noninvasive photoacoustic computed tomography of mouse brain metabolism in vivo. Neuroimage *64*, 257–266.

Yao, J., Kaberniuk, A.A., Li, L., Shcherbakova, D.M., Zhang, R., Wang, L., Li, G., Verkhusha, V.V., and Wang, L.V. (2016). Multiscale photoacoustic tomography using reversibly switchable bacterial phytochrome as a near-infrared photochromic probe. Nat. Methods *13*, 67–73.

Ye, S., Yang, R., Xiong, J., Shung, K.K., Zhou, Q., Li, C., and Ren, Q. (2012). Label-free imaging of zebrafish larvae in vivo by photoacoustic microscopy. Biomed. Opt. Express *3*, 360–365.

Yu, H., Farley, B.J., Jin, D.Z., and Sur, M. (2005). The coordinated mapping of visual space and response features in visual cortex. Neuron *47*, 267–280.

Yuste, R. (2015). On testing neural network models. Nat. Rev. Neurosci. *16*, 767.

Yuste, R., and Konnerth, A. (2005). Imaging in Neuroscience and Development: A Laboratory Manual (Cold Spring Harbor Laboratory Press).

Zago, S., Lorusso, L., Ferrucci, R., and Priori, A. (2012). Functional Neuroimaging: A Historical Perspective (InTech).

Zemp, R.J., Bitton, R., Li, M.L., Shung, K.K., Stoica, G., and Wang, L.V. (2007). Photoacoustic imaging of the microvasculature with a high-frequency ultrasound array transducer. J. Biomed. Opt. *12*, 010501.

Zhang, Q., Liu, Z., Carney, P.R., Yuan, Z., Chen, H., Roper, S.N., and Jiang, H. (2008). Non-invasive imaging of epileptic seizures in vivo using photoacoustic tomography. Phys. Med. Biol. *53*, 1921–1931.

Zhang, E.Z., Laufer, J.G., Pedley, R.B., and Beard, P.C. (2009). In vivo high-resolution 3D photoacoustic imaging of superficial vascular anatomy. Phys. Med. Biol. *54*, 1035–1046.

Zhang, X., Jiang, M., Fawzi, A.A., Li, X., Shung, K.K., Puliafito, C.A., Zhang, H.F., and Jiao, S. (2010). Simultaneous dual molecular contrasts provided by the absorbed photons in photoacoustic microscopy. Opt. Lett. *35*, 4018–4020.

Zhang, X., Zhang, H.F., Puliafito, C.A., and Jiao, S. (2011). Simultaneous in vivo imaging of melanin and lipofuscin in the retina with photoacoustic ophthalmoscopy and autofluorescence imaging. J. Biomed. Opt. *16*, 080504.

Zhao, M., Nguyen, J., Ma, H., Nishimura, N., Schaffer, C.B., and Schwartz, T.H. (2011). Preictal and ictal neurovascular and metabolic coupling surrounding a seizure focus. J. Neurosci. *31*, 13292–13300.